FEDERAL UNIVERSITY OF RIO GRANDE DO SUL
BRAZILIAN SYNCHROTRON LIGHT LABORATORY - LNLS
ENGINEERING PHYSICS

DEVELOPMENT OF A MULTIPURPOSE BIAXIAL TENSILE DEVICE FOR *IN SITU* STRUCTURAL CHARACTERIZATION USING SYNCHROTRON LIGHT

UNDERGRADUATE DISSERTATION

Anderson Bordin

Porto Alegre, RS, Brazil

2017

DEVELOPMENT OF A MULTIPURPOSE BIAXIAL TENSILE DEVICE FOR *IN SITU* STRUCTURAL CHARACTERIZATION USING SYNCHROTRON LIGHT

Anderson Bordin

Undergraduate Dissertation presented to the Engineering Physics Graduation Committee of Federal University of Rio Grande do Sul (UFRGS), in partial fulfillment of the requirements for the degree of

Bachelor of Science in Engineering Physics

Advisor at UFRGS: Prof. Dr. Fabiano Bernardi

Coadvisor at LNLS: Dr. Márcio Medeiros Soares

Porto Alegre, RS, Brazil

2017

Bordin, Anderson

Development of a multipurpose biaxial tensile device for *in situ* structural characterization using synchrotron light / by Anderson Bordin. – 2017.
64 f.

Advisor: Fabiano Bernardi
Coadvisor: Márcio Medeiros Soares

Undergraduate Dissertation - Federal University of Rio Grande do Sul, Institute of Physics, Bachelor of Science in Engineering Physics, Porto Alegre, BR-RS, 2017.

1. Instrumentation. 2. Tensile Device. 3. Synchrotron Radiation. I. Bernardi, Fabiano. II. Soares, Márcio Medeiros. III. Title.

e-mail: anderson_bordin@hotmail.com

Federal University of Rio Grande do Sul
Brazilian Synchrotron Light Laboratory - LNLS
Engineering Physics

The Examining Committee
approves the Undergraduate Dissertation

DEVELOPMENT OF A MULTIPURPOSE BIAXIAL TENSILE DEVICE FOR *IN SITU* STRUCTURAL CHARACTERIZATION USING SYNCHROTRON LIGHT

elaborated by
Anderson Bordin

in partial fulfillment of the requirements for the degree of
Bachelor of Science in Engineering Physics

EXAMINING COMMITEE:

Fabiano Bernardi, Dr.
(President/Advisor)

Cristiano Krug, Dr. (UFRGS)

Gustavo de Medeiros Azevedo, Dr. (UFRGS / LNLS)

Porto Alegre, February 2017.

Don’t worry about genius and don’t worry about not being clever. Trust rather to hard work, perseverance, and determination. The best motto for a long march is ’Don’t grumble. Plug on’.
You hold your future in your own hands. Never waver in this belief. Don’t swagger. The boy who swaggers – has little else that he can do. He is like a cheap-Jack crying his own paltry wares. It is the empty tin that rattles most.
Be honest. Be loyal. Be kind. Remember that the hardest thing to acquire is the faculty of being unselfish. As a quality it is one of the finest attributes of manliness.
Love the sea, the ringing beach and the open downs.
Keep clean, body and mind.

Sir Frederick Treves, Sergeant in Ordinary to HM the King, Surgeon in Ordinary to HRH Prince of Wales, written at 6 Wimpole Street, Cavendish Square, London, on September 2, 1903, on the occasion of the twenty-fifth anniversary of the Boy’s Own Paper.

ACKNOWLEDGMENTS

To my parents, Ivonice and Agenor, who always encouraged me. You gave me all the support to I reach my dreams. To you, my eternal gratitude;

To Fabiano, for accepting this challenge and sustaining my madness. Your guidance and adjustments have made this work more valuable;

To Márcio, by your confidence, teaching, patience, and for all the opportunities you presented me;

To LNLS/CNPEM, specially to XRD2 beamline colleagues Antônio and Douglas and also to Gustavo, for your patience and knowledge;

To Vanderson, the brother I did not have;

To João and Scopel and our friendship;

In special, to the *LSD group* Lívia, Carol, and Alef, by the fellowship, by the encouraging conversations and by the example of friendship. By the endless conversations and philosophies over the past five years. This period would have been somewhat tedious without you;

And to all of those that helped me to get here...

To all of you, my sincere thanks. I hope to be able to repay all the good and all the help that has been given to me.

The biaxial device is a ownership and common use equipment. All the knowledge here developed was fomented by LNLS/CNPEM resources.

to infinity... and beyond

— Buzz Lightyear

ABSTRACT

Undergraduate Dissertation
Engineering Physics
Federal University of Rio Grande do Sul

DEVELOPMENT OF A MULTIPURPOSE BIAXIAL TENSILE DEVICE FOR *IN SITU* STRUCTURAL CHARACTERIZATION USING SYNCHROTRON LIGHT

AUTHOR: ANDERSON BORDIN
ADVISOR: FABIANO BERNARDI
COADVISOR: MÁRCIO MEDEIROS SOARES

The knowledge of materials properties and the elucidation of the mechanical behavior of nanostructured thin films in comparison to their microstructure allows one to optimize the properties for applications in the industrial sector. In this way, it is possible to develop technological applications or enrich devices with new functionalities.

The present work is dedicated to design and to manufacture a tensile device able to stretch thin films, demonstrating the influence of traction on the microstructure of these films. The mentioned traction is used to induce structural deformations with changes in the interplanar distances at the atomic scale. This is the initial procedure of a long project which aims to control (due to the magnetocrystalline anisotropy) spin orientation in AFMs once the direction of the magnetic alignment depends strongly on the direction of deformation to which this film is subjected.

In this work, thin AFM films are produced (via sputtering deposition) and an equipment is built to study their atomic structure under stress. The mechanical properties (hardly accessible by other approaches) are derived from the microstructural information accessed by the X-ray diffraction technique. Besides it is explored and applied some concepts from *precision engineering* whose are going to be intensely used on Sirius (the newest Brazilian Synchrotron facility - under construction) sample stages environments.

Keywords: Instrumentation. Tensile Device. Synchrotron Radiation.

RESUMO

Trabalho de Diplomação em Engenharia Física II
Instituto de Física
Universidade Federal do Rio Grande do Sul

DESENVOLVIMENTO DE UM DISPOSITIVO DE TRAÇÃO BIAXIAL PARA CARACTERIZAÇÃO ESTRUTURAL *IN SITU* UTILIZANDO LUZ SÍNCROTRON
AUTOR: ANDERSON BORDIN
ORIENTADOR: FABIANO BERNARDI
CO-ORIENTADOR: MÁRCIO MEDEIROS SOARES

O conhecimento das propriedades dos materiais e a elucidação do comportamento mecânico de filmes finos nanoestruturados em comparação com a sua microestrutura permite optimizar as propriedades para aplicação no sector industrial. Desta forma, é possível desenvolver aplicações tecnológicas ou enriquecer dispositivos com novas funcionalidades.

O presente trabalho é dedicado ao desenho e fabricação de um dispositivo de tração capaz de esticar filmes finos, demonstrando a influência da tração na microestrutura destes filmes. A referida tração é utilizada para induzir deformações estruturais com alterações nas distâncias interplanares à escala atômica. Este é o procedimento inicial para um longo projeto que tem como objetivo controlar (devido a anisotropia magnetocristalina) a orientação de spin em AFMs uma vez que a direção do alinhamento magnético depende fortemente da direção de deformação à qual filmes finos são submetidos.

Neste trabalho, são produzidos filmes finos de AFM (via deposição por *sputtering*) e um equipamento é construído para estudar sua estrutura atômica sob stress. As propriedades mecânicas, dificilmente acessíveis por outras abordagens, são derivadas da informação microestrutural acessada pela técnica de difração de raio-X. Além disso, são explorados conceitos de engenharia de precisão e estabilidade mecânica pensando em requisitos a serem utilizados no Sirius (novo acelerador síncrotron, em construção).

Palavras-chave: Instrumentação. Dispositivo de Tração. Radiação Síncrotron.

LIST OF FIGURES

Figure 1.1 – Schematic view of a synchrotron lightsource. Electrons moving at highly relativistic speed emit electromagnetic (synchrotron) radiation as their direction is changed. Adapted from [3]. 17
Figure 1.2 – Schematic overview of XRD2 beamline at LNLS. Courtesy from XRD2 group. 18
Figure 1.3 – Tensile device from DiffAbs beamline. Adapted from [4]. 19
Figure 1.4 – AFM materials show alignment in a regular pattern with neighboring spins (on different sublattices) pointing in opposite directions. Adapted from [8]. 20
Figure 1.5 – The bulk CoO structure presents AFM behavior along the direction [111]. Adapted from [11]. 21
Figure 3.1 – Diffractometer of XRD2 beamline. Distance between the X-ray beam and the center of the Euler's circle (highlighted red) is about 60 mm. Adapted from [13]. 25
Figure 3.2 – Flexure hinge is a concept based on the mechanical stiffness of the materials, processed in such a way to allow relative flexibility without, however, causing fatigue effects. Adapted from [15]. 26
Figure 3.3 – Geometric entities that represent the permissible motion (rotation) and that contain the constraints to generate a flexure system with the desired motion. Adapted from [16]. 28
Figure 3.4 – Parasitic motion of a stage supported by two leaf springs subjected to a force. Adapted from [17]. 29
Figure 3.5 – Linear motion obtained from *Principle of Cancellation*. Adapted from [18]. 29
Figure 3.6 – Idealization of the 2D plane stress problem for numerical solution of a region Ω submitted to boundary conditions Γ. Adapted from [21]. 31
Figure 3.7 – Digital Image Correlation determines a transformation that leads from one image $C(x_0, y_0)$ to another $C'(x'_0, y'_0)$. Adapted from [26]. 35
Figure 3.8 – 50 μm Kapton substrate optical microscopy. 37
Figure 3.9 – Schematic view of SPM analysis. Adapted from [27]. 41
Figure 3.10 – Template X-ray reflectivity curve. Adapted from [28]. 42
Figure 3.11 – Definition of the scattering vector $\mathbf{Q}$ as a function of the incident wave vectors $\mathbf{K}_0$ and scattered $\mathbf{K}$. Adapted from [32]. 44
Figure 3.12 – Measurement θ-2θ of thin films probe flat crystals orientated along the surface. Adapted from [30]. 45
Figure 3.13 – Due the relative alignment of the sample to the detector, distinct scattering components from different crystallites orientations are being probed. 45
Figure 4.1 – Bending silicon monochromator sagittal crystal system (in disuse). Silicon crystal bracket has been replaced by the clamps; Kapton's rectangular sheet is stretched guided by a rotational movement performed by the system around a virtual plane (designing feature), changing thus the height of sample position. 48
Figure 4.2 – Reinforced leaf spring: the bending movement is fully realized by the thin parts. The reinforced part is assumed to be infinitely stiff, without suffering any change during bending. Adapted from [34]. 49
Figure 4.3 – TeDi last design version: it still requires verification of some details but it will be machined soon. 50

Figure 4.4 – TeDi is a partitioned machine. 50
Figure 4.5 – Deformation field (color scale in mm) of 2D substrate; arrows indicate the displacement on different regions. 52
Figure 4.6 – Kapton substrate 50 μm (right) and 75 μm thick (left) (10×10 μm^2). 53
Figure 4.7 – SPM images of films deposited on Si(100) substrate (S1, S2 and S3, respectively). 54
Figure 4.8 – The simulation of XRR from sample S2 (CoO* /Si) showing higher density than suspected; probable metallic Co occurrence. 55
Figure 4.9 – Usual θ-2θ ($\mathbf{q_z}$ scattering) experimental setup at XRD2 beamline. 56
Figure 4.10 – θ-2θ diffraction measurement of S1-Si100 sample (Ta / Si). Crystallization takes place in the β phase, presenting texturization [001]. 56
Figure 4.11 – Representative $\mathbf{Q_x}$ scattering setup at XRD2 beamline. 57
Figure 4.12 – Decrease in interplanar distance (decrease of lattice parameter **out-of-plane**) with increasing stress ($1/d_{hkl}^2 \sim 1/c^2$). 58
Figure 4.13 – Increased interplanar distance (increase lattice parameter **in-plane**) with increasing stress ($1/d_{hkl}^2 \sim 1/a^2$). 58
Figure 4.14 – Measurement of the scattering component **Q** out-of-plane $\mathbf{q}_z$; decrease of the interplanar distance when increasing the applied stress. 59
Figure 4.15 – Measurement of the scattering component **Q** in-plane $\mathbf{q}_x$; increase of the interplanar distance when increasing the applied stress. 59

LIST OF ABBREVIATIONS AND ACRONYMS

CNPEM	*Centro Nacional de Pesquisa em Energia e Materiais* (Portuguese)
DIC	Digital Image Correlation
DOF	Degree of Freedom
EDM	Electro-Discharge Machining
FACT	Freedom and Constraint Topology
FEA	Finite Element Analysis
LNLS	*Laboratório Nacional de Luz Síncrotron* (Portuguese)
LNNANO	*Laboratório Nacional de Nanotecnologia* (Portuguese)
SPM	Scanning Probe Microscopy
XRD	X-ray Diffraction
XRR	X-ray Reflectivity

LIST OF SYMBOLS

ρ	Density
E	Elastic (or Young's) Modulus
ν	Poisson's ratio
γ_{xy}	Shear Strain
τ_{xy}	Shear Stress
ϵ_x, ϵ_y	Strain in the x and y directions
σ_x, σ_y	Stress in the x and y directions

CONTENTS

1 INTRODUCTION 15
2 PURPOSES 23
3 METHODOLOGY 24
3.1 TENSILE DEVICE DESIGN 24
3.1.1 Forces and Motion 24
3.1.2 Size 25
3.1.3 Precision, Stability, and Motion 25
3.1.4 Bidimensional Finite Element Analysis (FEA 2D) 30
3.1.5 Digital Image Correlation 34
3.1.5.1 Image Matching and Optimization Criteria 35
3.2 DESCRIPTION OF SAMPLES AND EXPERIMENTAL TECHNIQUES 36
3.2.1 Polymeric Substrate 36
3.2.2 Sputtering Deposition and Sample Description 38
3.2.3 Scanning Probe Microscopy technique (SPM) 40
3.2.4 X-ray Analysis Techniques 41
3.2.4.1 X-ray Reflectivity - XRR 41
3.2.4.2 X-ray Diffraction - XRD 43
4 RESULTS AND DISCUSSIONS 47
4.1 FLEXURE DEVICE 47
4.2 FINITE ELEMENT ANALYSIS 51
4.3 SCANNING PROBE MICROSCOPY MEASUREMENTS 53
4.4 XRD and XRR MEASUREMENTS 54
5 CONCLUSIONS 60
6 PERSPECTIVES 61
REFERENCES 62

1 INTRODUCTION

By the beginning of the twentieth century, all problems in physics seemed to be solved. Scientists believed that they understood the most fundamental principles of nature: atoms were building blocks and people relied on the Newtonian laws of motion. However, scientists gradually realized that their knowledge was far from complete, culminating in new theories, among them *quantum mechanics* and its purpose in describing certain features of matter behavior observed on the atomic and subatomic scale.

The American physicist Richard Feynman on their *There's Plenty of Room at the Bottom* talk on December, 1959 considered the possibility of manipulation of individual atoms and the making of nanoscale machines. The talk went unnoticed and didn't inspire advances till the 1990s, when it was rediscovered and published as a fundamental event, being nowadays considered as the starting point in the nanotechnology history [1].

In the middle of 1970s, the concept of nanoscience and nanotechnology arose as the study, manipulation, and application of matter at atomic and/or molecular scale, in dimensions in the order of a billionth part of a meter, that is, 1 nm (1×10^{-9} m) [2]. Materials at the nanoscale (by definition, materials that have one dimension smaller than 100 nm) show properties significantly altered compared to the bulk material, and these are best described by the quantum theory. The understanding on how to synthesize and to characterizing nanomaterials/nanostructures to get special features represents the real breakthrough at the atomic scale.

In this way, characterizing and evaluating the quality and performance of nanomaterials supports real innovation in the scientific and industrial sectors. Nowadays scientists and engineers are working on a wide variety of methods to synthesize nanomaterials and to take advantage of their enhanced properties. For such purpose, the application of knowledge of physics, chemistry, mathematics and engineering in the research and development of materials and technologies is required. Therefore, distinct materials analysis is required depending on which specific property is under investigation.

The initial *boom* in nanotechnology in the 1980s brought new motivation and touched on previously unmet needs: to achieve new responses, new experiments had to be thought out, and along with new models and predictions, high-precision scientific instruments were developed. Some of the most common methods used to characterize nanomaterials are based on X-ray techniques.

In this context, synchrotron light sources represent unique tools to study nanomaterials. Since their discovery in late 1895 by Wilhelm Röntgen, X-rays have played a crucial role in the society development. As soon X-rays were discovered, many researchers focused their research on the study and application of X-rays. One important discovery was the use of X-rays to elucidate the crystal structure of materials and in the investigation of important scientific issues, such as the DNA discovery and the mechanism by which it replicates [3].

Specifically, on materials analysis studies, the use of X-rays is justified once they are able to probe deeply and non-destructively solid materials. In addition, X-ray photons with energies of several keV have wavelengths comparable to those of typical atomic spacing in solid materials, that is a few angströms (1 Å $= 10^{-10}$ m).

A particular and efficient way to obtain X-ray photons is by the use of synchrotron sources. When electrons moving close to the speed of light are forced to change their direction under the action of a magnetic field (generated, for example, by the bending magnet dipoles placed at the end of straight sections of a storage ring) occurs the emission of electromagnetic radiation with specific features. In Synchrotron sources the bending magnet dipoles are placed at the end of straight sections of a storage ring. As can be seen in figure 1.1 [3], the electrons, here presented as blue spheres, are obtained from an electron source and primarily accelerated in a linear accelerator (not showed here). When having a given energy they are injected in the storage ring and accelerated to a final energy of the order of GeV in a circular path (the vacuum storage ring). The storage ring is composed by quadrupoles and sextupole responsible for focusing the electron beam (compensating Coulomb repulsion) and to correct chromatic aberrations that arise from the focusing by the quadrupoles, respectively.

The storage ring is composed of by a sum of straight sections where at the end is located the beamline (the link between the storage ring and experimental station). At the end of the straight sections exists the mentioned bending magnetic dipoles, which changes the direction of the electron beam. This bending movement allows the emission of the so-called *synchrotron light* in a narrow cone in the forward direction, tangent to the electron's orbit. Besides magnetic dipoles, wigglers or undulators are other possible insertion devices used to obtain higher photons' flux at the sample position. Emerging radiation from storage ring is a polychromatic radiation; the focusing optics is responsible for selecting beam energy (monochromator mirror) and correcting beam divergences (focusing optics, similarly geometric optics) to set a given beam size at the sample [3] .

Synchrotron light source presents several important characteristics, such as the emission of light in a wide range of frequencies (from the far IR to hard X-rays) [3]. Moreover, the brightness emitted from the synchrotron source is many orders of magnitude greater than that produced by conventional X-ray sources (between 6 and 10 orders of magnitude higher than those produced by laboratory sources). It also has low beam emittance (low particle spread in position-and-momentum phase space) and short pulse length (usually under 1 ps), allowing time-resolved experiment executions.

These characteristics allow one performing experiments with improved time and spatial resolution and better signal to noise ratio.

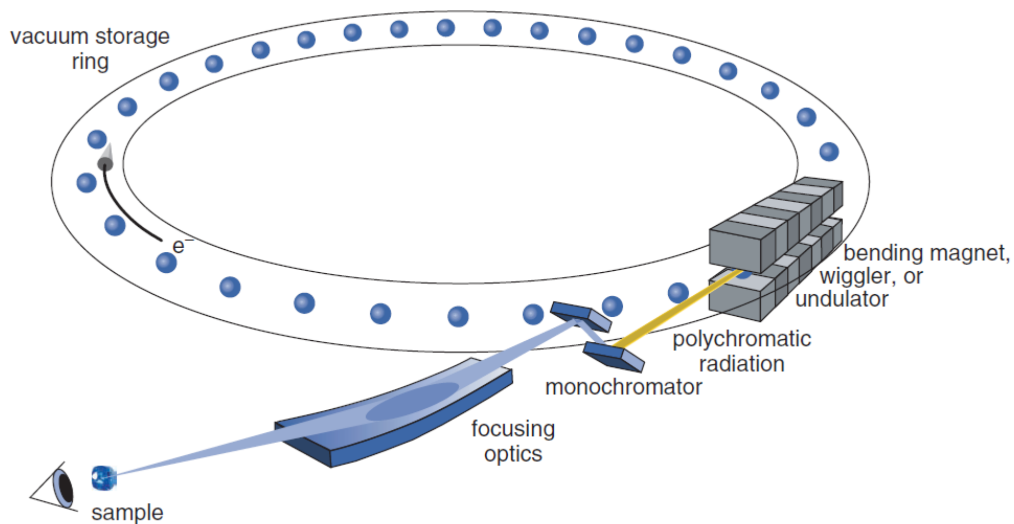

Figure 1.1: Schematic view of a synchrotron lightsource. Electrons moving at highly relativistic speed emit electromagnetic (synchrotron) radiation as their direction is changed. Adapted from [3].

There are several synchrotron light sources around the world. The second-generation synchrotron light source, named UVX accelerator of LNLS (the Brazilian Synchrotron Light Laboratory) was designed and built during the 80s and the 90s, and came into operation in 1997, being the only particle accelerator of such kind in Latin America. Currently, the Brazilian Synchrotron has 15 operational beamlines, covering energies ranging from below to 1 eV (infrared) to tens of keVs, depending on their design and experimental goal. The principal uses include X-ray Diffraction (XRD), Macromolecule Crystallography, Small Angle X-ray Scattering (SAXS), X-ray Absorption and Fluorescence Spectroscopy (XAS and XRF) and X-ray Photoelectron Spectroscopy.

Among several modern techniques, scattering techniques are widely used (diffraction and reflectivity, in particular, were the most used techniques during this project). The use of

X-rays scattering techniques allows to probe non-destructive solid materials and to accurately measure thicknesses and interatomic spacing [3].

The XRD2 beamline at LNLS is dedicated to run experiments of X-ray scattering techniques. It is a 1.67 T bending magnet beamline and the optics is composed of a Rh-coated vertical focusing mirror and a sagittal-focusing Si(111) double-crystal monochromator (see figure 1.2 for better understanding). Its main applications are in solid state physics, chemistry, and biology. Several types of measurements can be made using this beamline: a wide range of diffraction/scattering techniques are possible in different sample environments, facilitated by the versatile 6+2 circles diffractometer.

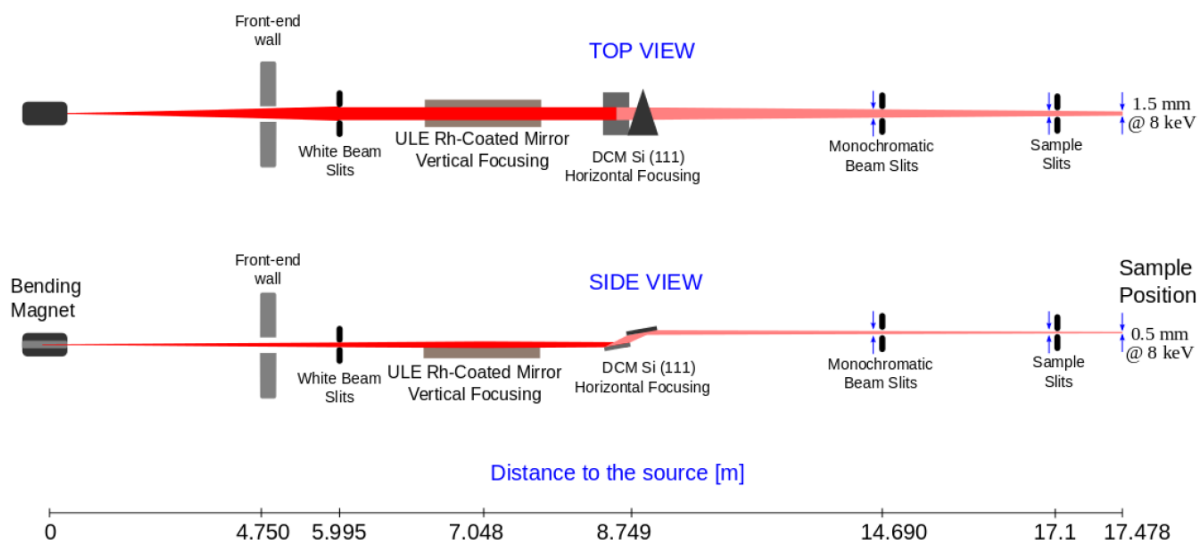

Figure 1.2: Schematic overview of XRD2 beamline at LNLS. Courtesy from XRD2 group.

A current worldwide scientific interest is the link between two distinct worlds: the *macroworld* and the *nanoworld*. The initial boom of nanotechnology at the 1980s gave new scientific motivation to researchers and brought some technical needs to be considered: since new experiments should be performed, instrumentation of high precision had to be developed. Scientific centers were created and high-tech engineering devices were designed aiming to probe physical effects at the nanoscale.

As mentioned, at the nanoscale the materials properties are significantly altered if compared to the properties at the macroscopic scale and commercial instruments do not fulfill the needs, which implies in manufacturing dedicated devices able to explore properties at this scale. This work proposes to engineer a device that allows conducting experiments using synchrotron light in thin films submitted to mechanical traction.

The proposed device is analogous to a commercial tensile test machine, which (with dimensions of meters) is designed to probe macroscopic mechanical properties of massive materials in the form of specimens.[1]

The mechanical properties of a material are directly related to its nanostructure. In the case of thin films, the same relation between microstructure and mechanical properties is valid, and becomes increasingly relevant in the development of new applications, as is the case of flexible electronics. The study of mechanical properties of thin films supported by flexible substrates, difficult to access by traditional methods, is feasible through X-ray diffraction experiments in samples subjected to traction, which directly probes the effect of traction on the microstructure of the thin films. These experiments involve the fabrication of a device capable of stretch different materials (usually polymer sheets) with high precision, reproducibility and a wide range of load, being versatile, light and small enough to be adapted to the diffractometer. This versatility implies that other materials can also be analyzed, which have already been successfully tested in experiments in the XRD2 beamline.

The design of such apparatus is based on an instrument developed on the DiffAbs beamline at SOLEIL, a French synchrotron facility (see figure 1.3), where the purpose is to verify mechanical properties of nanostructured thin films deposited on polymeric substrates [4].

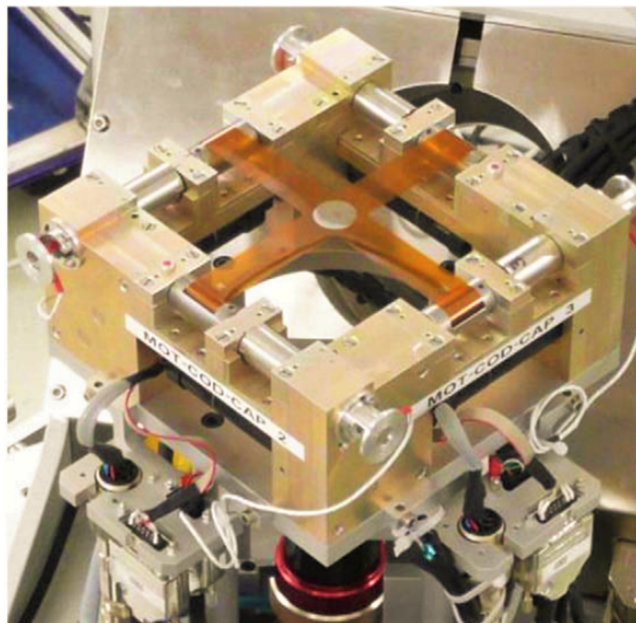

Figure 1.3: Tensile device from DiffAbs beamline. Adapted from [4].

[1] To probe mechanical properties, tests require measuring the response of the material to a given applied force. Uniaxial stress testing machines are used to obtain the mechanical characteristics of isotropic materials. For anisotropic materials, biaxial tests are performed, both usually under extreme conditions.

Understanding the behavior of matter and its magnetic characteristics in distinct materials (and nanostructures) represents the potential for greater technological impact: solid state quantum computing is a visible advance, as well a new generation of magnetic RAM memories and high-density memory devices [5].

From the fundamental understanding point of view, the focus is to study thin films with great potential in spintronics. Spintronics is the area of physics of condensed matter that studies the spin properties of electrons, giving it new technological applications or enriching electronic devices with new functionalities [6].

While ferromagnetic materials (FM) are formed by atoms whose magnetic moments have a spontaneous tendency to parallel alignment, antiferromagnetic materials (AFM) have magnetic moments of atoms or molecules aligned in a regular pattern with neighboring spins (in different sublattices) pointing in opposite directions (see figure 1.4). They are internally magnetic, but their microscopic moments alternating between neighboring atomic sites result in liquid magnetic moment equal to zero [7].

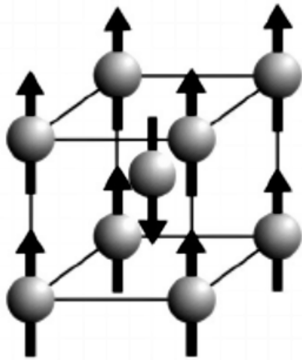

Figure 1.4: AFM materials show alignment in a regular pattern with neighboring spins (on different sublattices) pointing in opposite directions. Adapted from [8].

The mentioned characteristic makes AFMs practically invisible to external magnetic fields, resulting in great difficulty in manipulating magnetic moments. However, spintronics by antiferromagnet materials is nowadays feasible [9].

An existing possibility to manipulate the orientation of spins in an AFM is to act on the *magnetocrystalline anisotropy* of the material. In general, anisotropy is a directional tendency of a physical property of a material. In magnetic materials (FM or AFM) the symmetry of the crystalline structure influences the electronic orbitals which, through the spin-orbit interaction, causes the occurrence of preferred axes of magnetization, or magnetocrystalline anisotropy. This preference in the orientation of the magnetic moments is associated with a magnetocrys-

talline anisotropy energy, minimized when the magnetic moments are oriented along these axes, the so-called *easy* magnetization axes.

Since the magnetic moment of AFM materials is hardly accessible by magnetic fields, one of the methods proposed to overcome this technological challenge is to act indirectly on the magnetic orientation. It can be performed by influencing the magnetocrystalline anisotropy through the deformation in the crystalline structure in order to disturb the magnetic equilibrium. If doing it in a controlled and reproducible way it is possible to access and to control the orientation of spins in AFMs.

In view of the potential application of information technology, different combinations of FM and AFM materials have been tested over the last few years. Given its high magnetocrystalline anisotropy, cobalt oxide (CoO) is among the most interesting AFM materials for spintronic devices and is therefore of great interest. CoO behaves as AFM below 289 K and crystallizes in the *rock salt* structure of NaCl (see figure 1.5) having Co and O planes that alternate along the direction [111] in a hexagonal lattice [10].

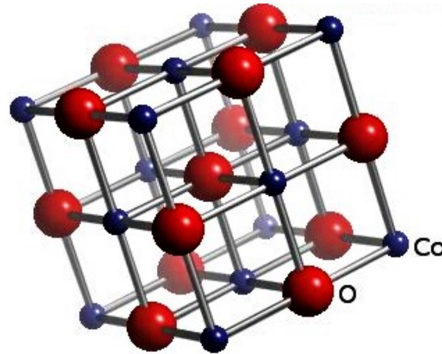

Figure 1.5: The bulk CoO structure presents AFM behavior along the direction [111]. Adapted from [11].

The CoO crystal structure is cubic above the Neel temperature (289 K). Below 289 K, the exchange interaction effect becomes dominant against randomization due to thermal effects, leading to the antiparallel ordering of neighboring magnetic moments (characteristic of AFM materials). The AFM transition is accompanied by a structural transition, modifying the lattice from cubic to monoclinic: relative elongation leads to the appearance of a perpendicular c axis (out-of-plane), distinct from a axis (in-plane).

For the case of a film of CoO grown epitaxially on different substrates, it was observed [12] that the direction of the magnetic anisotropy depends strongly on the direction of deformation to which this film is subjected. When the deformation is compressive in the plane (e.g. CoO/Ag(001)), the ratio $c/a >> 1$ implies planar anisotropy (the spins are oriented in-plane of

the film). In turn, an extensive deformation (e.g. CoO/MnO(001)), with $c/a << 1$ leads to a perpendicular anisotropy (the spins oriented out-of-plane of the film). The expectation is that the influence of the traction (stress) on the microstructure of the CoO affects its magnetocrystalline anisotropy, being the traction used in the control of spin orientation in AFMs, similar to the deformations caused from the epitaxy.

2 PURPOSES

The continuous improvement process that is provided by the staff of the beamlines at LNLS is responsible for maintaining and supplying new sample environments and new measuring setups to users. Dedicated instruments are thought and developed to realize studies with X-ray techniques existing at LNLS.

The tensile device development aims to offer to the LNLS facility a scientific instrument capable of stressing elastic/flexible substrates with the expectation of causing microstructural changes in thin films grown on them. In particular, the control of spins orientation in AFMs is a challenge, and a control method is proposed for deformations in the crystalline structure at the atomic scale, which acts on the magnetocrystalline anisotropy of this type of material.

In addition to controlling the microstructure through a tensile instrument, understanding the growth mechanism of thin films through sputtering deposition, especially CoO films, is also a proposed goal. The films are deposited on flexible substrates and understanding the adhesion of the sample to the support material ensures effectiveness in the load transference. The intention is to understand and to control parameters related to the deposition process to obtain higher quality and textured films (preferential crystalline orientation), avoiding the formation of undesired non-stoichiometric (Co_xO_y) phases.

In this work is proposed the design and manufacture of a tensile device for rectangular (1D) and cruciform (2D) format substrates to be initially used in the XRD2 beamline but which is versatile in order to be adaptable to other UVX-LNLS beamlines.

An important requirement for diffraction experiments is to avoid *shadow effects* at the entrance and exit of the incident and diffracted X-ray beam, respectively. The design must predict that the entire upper hemisphere defined by the film will be clear of obstacles. The multipurpose character intends to attend to different scientific cases of the LNLS users community (absorption and small angle X-ray scattering (SAXS)), being it a characteristic always regarded in the instrumentation development.

The design of the traction device will not only integrate the XRD2 and other beamlines into the LNLS. This will be used as a prototype for CARNAÚBA samples environment, the SIRIUS nanofocus beamline (under construction). This scenario imposes requirements: size, mechanical stability and low power dissipation (heat) are the main parameters studied and considered during the design of the prototype.

3 METHODOLOGY

The project cover two distinct challenges that interrelate with the larger goal: the **engineering challenge** in designing mechanical equipment and the **scientific challenge** to understanding the magnetic, structural and mechanical properties of AFM thin films. The experimental procedure comprises certain key steps to achieving specifications aiming a precision and exclusive design.

3.1 TENSILE DEVICE DESIGN

The experimental procedure requires determining the technical specifications needed for the design of the tensile device. The following criterion and approach are adopted:

3.1.1 Forces and Motion

Initially, mechanical variables like forces and torques needed to substrate traction were dimensioned aiming to understand and specify stresses to be supplied by the device. Then, the better mechanical approach which should be used was determined. Parameters like size, mechanical stability, and thermal dissipation are under consideration.

After some approaches, it was established that linear guides and ball bearings rails could not be used: they support the imposed torques but do not fit the scalability goal. Solution based on pneumatic components was suggested but technical considerations (higher power dissipation, harder implementation, and control) invalidated its use.

Effects related to static and dynamic friction are pertinent and came to account. Interrogations about the way by the thin films should be clamped to the tensile frame or even "locking" effects (observed when occurs a change in the direction of the load applied to any surface and it is related to the static friction) were computed on an *error budget* list.

The 2D traction and diffraction experiments require a completely free upper hemisphere (avoiding shadow effects to X-ray beam), implying that the sample must be located above from the traction plane.

3.1.2 Size

The model that will be assumed as a starting point was developed in DiffAbs experimental station at SOLEIL synchrotron source. That machine is reasonably compact with a cast of the central region and hemisphere of the film without obstacles, allowing X-ray diffraction experiment (no shadowing edges) (see figure 1.3) [4]. Two couples of motors (whose can be actuated separately in order to keep load homogeneity) and force sensors are fixed to the device frame. The force sensors are calibrated in the range of 0 – 200 N.

The DiffAbs device was designed to attend a different purpose and represents poorly what should be implemented at LNLS: its environment supports a big and heavy apparatus and it is designed to deal with polymeric substrates. Besides XRD2 size constraints (see figure 3.1), the conceptual design must allow resizing, hardly achievable from DiffAbs' design.

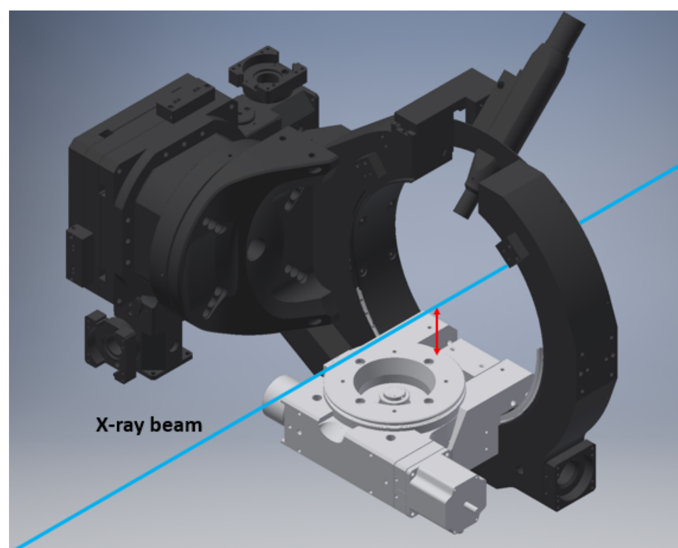

Figure 3.1: Diffractometer of XRD2 beamline. Distance between the X-ray beam and the center of the Euler's circle (highlighted red) is about 60 mm. Adapted from [13].

3.1.3 Precision, Stability, and Motion

After understanding both the scope of the work, as well the structure available at the CNPEM and the demands around the tensile device, it was established the concept that fits the needs of XRD2 (UVX-LNLS) and the future SIRIUS' facilities. This concept is based on the use of **flexure guides** with hinge behavior. A flexible hinge is a mechanical member that provides relative rotation between adjacent rigid members by flexing (bending) without, however, cause overstress condition or fatigue in the material [14].

Flexure hinges are fabricated by removing material from a blank piece. The manufacturing processes that are being utilized for this purpose include end-milling, electro-discharge machining (EDM), laser cutting or metal stamping in the case in dealing with metals structures. The flexure hinge behavior consists of an elastically flexible region between two rigid parts that must undergo relatively limited rotation in a mechanism (called *compliant* due to the presence of at least one flexure hinge) that is supposed to achieve a task (see figure 3.2).

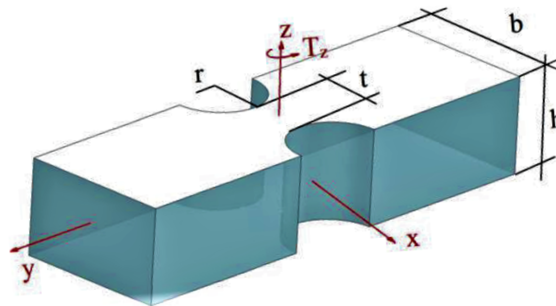

Figure 3.2: Flexure hinge is a concept based on the mechanical stiffness of the materials, processed in such a way to allow relative flexibility without, however, causing fatigue effects. Adapted from [15].

The required precise motion is eminent to the current project. Flexure hinges systems are required because of the negligible friction, (relatively) ease of manufacturability, durability and large angular ranges, besides their continuous mechanical design optimization by Finite Element Analysis (FEA). However, the flexibility of these hinges makes modeling very complex and specific to the particular engineering applications for which they were developed. It presents deterministic movement and according to the imposed geometry, minimizing degrees of freedom (DOFs) translates in fine movement.

The flexure hinges features can be summarized as follow [15]:

- No friction losses;
- No need for lubrication;
- No hysteresis behavior;
- Capacity to be utilized in small-scale applications;
- Ease of fabrication;
- Virtually no maintenance needed;
- Nanometer accuracy (if adequately designed).

However, flexure hinges also have limitations [15]:

- Relatively low levels of rotations (not exactly a limitation);

- The rotation is not a pure movement;
- The flexure hinge is usually sensitive to temperature variations (dimensions change as a result of thermal expansion leads to modifications in the calculated compliance values);
- Residual stresses can create asymmetries leading to parasitic motions.

As mentioned, flexure hinges modeling is very complex and specifics projects are developed to particular applications. In general, regardless of the DOFs, flexure based devices are often designed via iteration and many designers are fortunate if they are able to synthesize one or two new concepts that possess only the specified motions.

The generation of multi-DOF flexure system concepts is difficult because typically there are several components that provide constraints in several directions while allowing motions in many other directions. It is difficult to visualize how the constraint and freedom lines within a complex flexure system relate to each other.

Although offering a number of advantages, compliant mechanisms present several challenges and disadvantages in some applications. Perhaps the largest challenge is the relative difficulty in analyzing and designing compliant mechanisms. However, a design principle is known as *Freedom and Constraint Topology (FACT)* represents a powerful method for the synthesis of the multi-DOF design of flexure based devices. FACT is based upon sets of geometric entities that contain quantitative information about a flexure system characteristics. It can be used to visualize the quantitative relationships between all possible flexure designs and all possible motions for a given design, which enables the unique mapping of freedom and constraint spaces [16].

Flexure systems consist of a combination of rigid and flexural elements whose are arranged and interconnected in a way that their compliant directions permit specified motions and their stiff directions prevent motions in all other directions. FACT makes possible to visualize and to determine the general shape(s) that a flexure system must have in order to permit specified motions. Moreover, it contains all of the relevant quantitative information that is needed to rapidly sketch, without complications when detailed mathematical treatments for optimization arise.

The FACT method contains a set of information about the flexure system's DOFs (freedom topology space) and a set about the flexure system's geometry (constraint topology). By the *principle of complementary topologies* (a mapping between freedom and constraint topologies), a unique mapping of the first set (DOFs) to the second set (geometry) is established.

The design procedure can be summarized as follow:

1. Specify the geometric entity (freedom topology) that represents the required movement;
2. Identifies which freedom space (FS) this topology belongs;
3. The principle of complementary topologies determines the geometric entities (from constraint space - CS) to flexure systems that permit the specified DOF.

To better understanding, see figure 3.3 below.

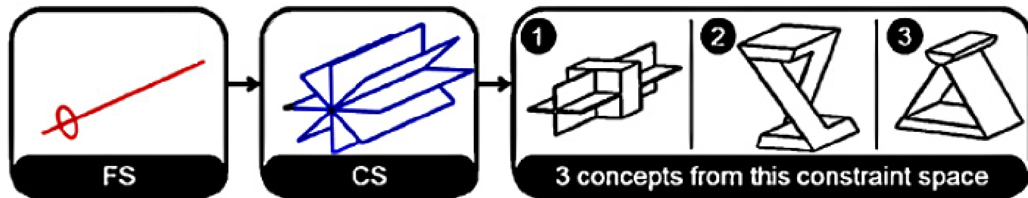

Figure 3.3: Geometric entities that represent the permissible motion (rotation) and that contain the constraints to generate a flexure system with the desired motion. Adapted from [16].

A rigid body has six DOFs. Any non-redundant constraint removes a DOF. Mathematically:

$$R = 6 - C \tag{3.1}$$

where C is the number of non-redundant constraints and R is the number of DOFs. A constraint is idealized as providing resistance to motion along its line of action, i.e. vectors which are mathematically independent.

The designer may use the catalog of matching freedom-constraint spaces to select the appropriate constraint spaces (design type) that may be used to synthesize the desired freedom space (DOF). That is, a designer may diagnose the DOFs that a flexure permits by finding the constraint space that the flexure fits within, and then looking up the matching freedom space.

After the minimum number of constraints has been selected via equation 3.1, additional constraints may be selected from within the constraint space (which guarantees to allow the desired DOFs) if it was necessary to improve the load capacity, symmetry, thermal stability and/or the stiffness of the flexure system in some, or all, of the constrained directions.

The flexure based device designed to the XRD2 project must present exclusively 1D movement. The desired pure translation is obtained by a topology which contains five non-

redundant constraints and one DOF. However, even using FACT method, when a stage is supported by a structure which has its stiffness reduced to determine one DOF (leaf springs, for instance), obligatorily occurs a rotational parasitic motion (see figure 3.4).

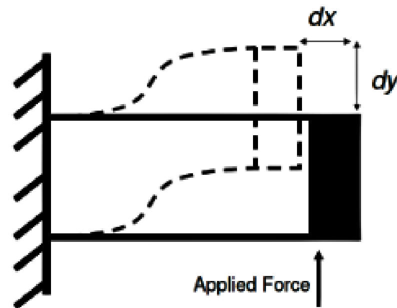

Figure 3.4: Parasitic motion of a stage supported by two leaf springs subjected to a force. Adapted from [17].

These parasitic movements can be canceled using the philosophy established by the *Cancellation or Compensation Principle*: when a second structure with the same motion (low stiffness to a specific direction), but now in the opposite direction is coupled to the first stage, it compensates the undesired parasitic displacement. Thus, introducing a second parasitic motion causes a relative motion (front to the reference frame) which implies a cancellation to those undesired movements, except to those translational (required) [18].

As can be seen at figure 3.5, with that construction the stiffness at both not desired motion directions is increased, remaining only the translational 1D motion (with features from FACT method still fulfilled).

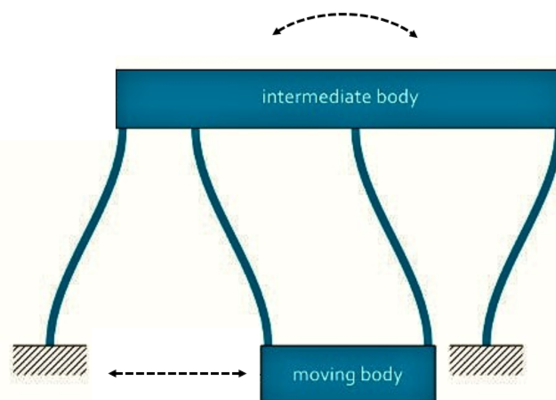

Figure 3.5: Linear motion obtained from *Principle of Cancellation*. Adapted from [18].

The precise movement needs for the traction of the flexible substrates is obtained by the action on the flexure structure, on which the flexible substrate is fixed: stepper motors adapted to gearboxes act as *linear actuators* and ensure that the flexure is moved with near to

micrometric precision and, therefore, also the substrate (which are strongly linked to flexure). Power consumption is low due to the combination of a gearbox and leadscrew (power screw) coupled to the step motors. It remains stationary (off) while the load being supported by the screw. The presented concept fits the limitations of dimension, precision, and heat dissipation.

The precision required in the manufacturing of the device, however, implies an increase in costs given the need to use the electro-discharge machining (great ratio aspect on device frame). The higher cost (around R$5000,00, or $1500,00, to the design here proposed) is justified since all the mechanical requirements are met and the project will provide an exclusive instrumentation. Given the challenging stability and accuracy requirements to the CARNAÚBA beamline, such a flexure-based construction will work as a conceptual test and will allow identification of (possible) impasses.

3.1.4 Bidimensional Finite Element Analysis (FEA 2D)

Finite Element Analysis (FEA) is a numerical technique for finding approximate solutions to boundary value problems for partial differential equations. FEA subdivides a problem into smaller, simpler parts (the called finite elements), with each subdomain represented by a set of element equations to the original problem.

The finite element analysis is a numerical method able to determine the evolution in the dimensions of a body against some physical phenomena (thermal gradient, electric, mechanical, etc.) induced by an external agent. The proposed structure is partitioned into small subdivisions which are treated as rigid and immutable elements (called finite elements) whose interaction is governed by a set of equations. The whole 3D is systematically recombined, grouping the elements into a global system of equations for the final calculation of the structure. Each subdivision is related to each other by gradients that take the simple mathematical format **k * x**, where **k** is a proportionality constant that imposes continuous and smooth transitions of physical states between neighboring subdomains and **x** the "reach" of interaction.

The continuum-based structural finite elements were invented in the aircraft industry during the early 1950s to solve problems when it arose in the design and analysis of aeronautical components. All of these pioneers were in the aerospace industry given that FEA is the confluence of some ingredients, one of which is a digital computation, and only large industrial companies (as well as some government agencies) were able to afford mainframe computers during the 1950s [19].

The general procedure to perform FEA is described as follow:

- Physical model: describe the problem simplifying a real engineering problem into a problem that can be solved by FEA;
- FEA model: discretize (mesh) the solid, define material properties, apply boundary conditions;
- FEA theory: choose approximate functions, formulate linear equations, and solve equations;
- Results: obtain, visualize and explain the results.

As mentioned, FEA is a powerful technique able to predict structural behavior before manufacturing of a component and so prevent not desired events yet on project stage. A branch of FEA theory is devoted to deal with those constructions whose the third dimension (the z-dimension) is clearly negligible once the thickness is quite small when compared to other dimensions in the reference XY plane (the stress vector is zero across a particular surface).

A state of deformation where there is no displacement in the z direction (the stresses related to z coordinates are assumed to be very small and not considered in the formulation) and whose displacements in the x and y directions are functions of only effects caused by traction/compression in this plane is called plane deformation. The finite element method in 2D structures (see figure 3.6) therefore, is restricted to the resolution of an adapted partial differential equation, with boundary conditions exclusively in the XY plane [20].

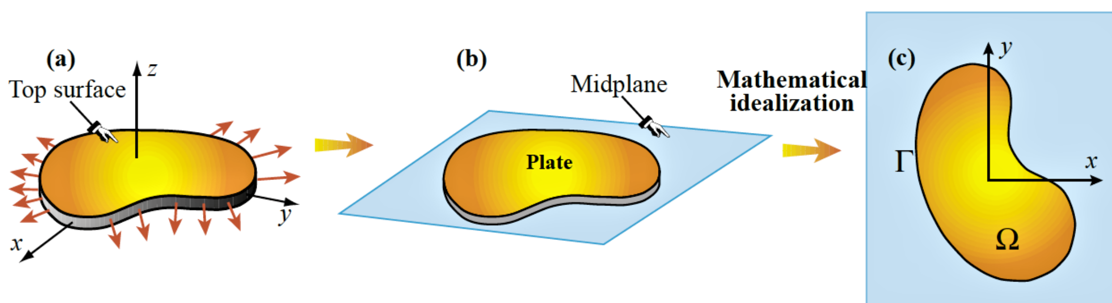

Figure 3.6: Idealization of the 2D plane stress problem for numerical solution of a region Ω submitted to boundary conditions Γ. Adapted from [21].

When that situation occurs over an entire element of a structure (the case for thin plates that are acted upon only by load forces that are parallel to them) the stress analysis is considerably simplified, as the stress state can be represented by a tensor of dimension 2 (representable as a 2×2 matrix).

In structural mechanics, the equations relating stress and strain arise from the balance of forces in the material medium. The plane stress problem considers two global displacements, u and v. Strains are obtained by derivation of displacements.

The stress-strain relation can then be written, assuming isotropic conditions

$$\begin{pmatrix} \sigma_x \\ \sigma_y \\ \tau_{xy} \end{pmatrix} = \frac{E}{1-\nu^2} \begin{pmatrix} 1 & \nu & 0 \\ \nu & 1 & 0 \\ 0 & 0 & \frac{1-\nu}{2} \end{pmatrix} \begin{pmatrix} \epsilon_x \\ \epsilon_y \\ \gamma_{xy} \end{pmatrix} \tag{3.2}$$

where σ_x and σ_y are the normal stresses in the x and y directions, and τ_{xy} is the shear stress. The material properties are expressed as a combination of E (the elastic modulus or Young's modulus) and ν, the Poisson's ratio.

The deformation of the material is described by the displacements in the x and y directions, u and v, from which the strains are defined as

$$\begin{aligned} \epsilon_x &= \frac{\partial u}{\partial x} \\ \epsilon_y &= \frac{\partial v}{\partial y} \\ \gamma_{xy} &= \frac{\partial u}{\partial y} + \frac{\partial v}{\partial x} \end{aligned} \tag{3.3}$$

The balance of force equations are

$$\begin{aligned} -\frac{\partial \sigma_x}{\partial x} - \frac{\partial \tau_{xy}}{\partial y} &= kx \\ -\frac{\partial \tau_{xy}}{\partial x} - \frac{\partial \sigma_y}{\partial y} &= ky \end{aligned} \tag{3.4}$$

where *kx* and *ky* are volume forces (body forces).

Combining the preceding relations, we arrive at the displacement equations, which can be written

$$-\nabla \cdot (\mathbf{c} \otimes \nabla \mathbf{u}) = \mathbf{k} \tag{3.5}$$

where **c** is a rank four tensor

$$c_{11} = \begin{pmatrix} 2G+\mu & 0 \\ 0 & G \end{pmatrix}$$

$$c_{12} = \begin{pmatrix} 0 & \mu \\ G & 0 \end{pmatrix}$$

$$c_{21} = \begin{pmatrix} 0 & G \\ \mu & 0 \end{pmatrix}$$

$$c_{22} = \begin{pmatrix} G & 0 \\ 0 & 2G+\mu \end{pmatrix}$$

where G, the *shear modulus*, is defined by

$$G = \frac{E}{2(1+\nu)} \tag{3.6}$$

and μ in turn is defined by

$$\mu = 2G\frac{\nu}{1+\nu} \tag{3.7}$$

$$\mathbf{k} = \begin{pmatrix} k_x \\ k_y \end{pmatrix} \tag{3.8}$$

and **k** are *volume forces*.

This is an elliptic partial differential equation (PDE) of system [20].

Specifically to the tensile device problem the finite element study allows to evaluate which geometries are most suitable to obtain regions with a greater homogeneous distribution of deformations and possible rupture points for the aimed range of forces. The rectangular (1D load) and cruciform (2D load) substrates can be used for studies of different deformation conditions. To verify the feasibility and optimize the substrates shape, FEA guarantees the usability of the proposed formats.

The potential use of the tensile device requires that the tensioned tape, whether polymeric or metallic, be subjected to stretches (ΔL/L) of up to about 5%. Due to the multipurpose application, the range of forces for the device goes up to 200 N, corresponding maximum tensions of 10^9 Pa. Some structural components (bearings and screws) are subjected to the mentioned forces, being dimensioned for such.

The simulations are performed using the Partial Differential Equation Toolbox existing on Matlab 2016a [22] which allows enter the desired geometry and compute a number of interesting quantities, such as the x- and y-direction strains and stresses and shear stress. The meshing mode used was the *Delaunay Triangulation* algorithm, which maximizes the minimum angle of all the angles of the triangles in the triangulation, already implemented in Matlab. It is important to note that the model requires boundary conditions related to the force applied to each substrate "arm". However, the relevant material feature to sustain the model is the stress (the force applied perpendicular to the surface of an object per unit area over which that force is distributed) which annuls geometric contributions and implies in a universal model. Thus, the boundaries conditions used on simulation must be the force (at each arm) associated with the stress able to cause deformation ΔL/L.

3.1.5 Digital Image Correlation

Historically synchrotron facilities are multiuser laboratories having a multipurpose philosophy. The tensile device also follows this argument: different materials are going to be tested, implying in a wide range of required load. Dealing with different materials at distinct shapes imply on difficulties in the reproducibility and reliability of the stress caused by the device so that a motion control based on the position of the stepper motors and that initial substrate geometry is probably insufficient.

When a usual tensile test is being executed, it is controlled by strain: strain gages or extensometers are used. However, an another and effective way to feedback the control system (which is also employed to measure deformation) is the optical solution Digital Image Correlation (DIC) [23].

DIC is an image analysis method based on gray value digital images used to measure in-plane full-field displacement fields of sample surfaces from an object under stress. It consists in registering pictures shot at different stages of loading that are processed subsequently: the proposed application is to detect small stretch variations [24] that occurred between two load stages, achievable by image comparison.

The conceptual understanding of image correlation is supported by *image matching*, a discipline of computer vision related to a large number of practical applications (industrial process control, automatic recognition, video compression and autonomous robots). Nevertheless, there is a great challenge to DIC implementation: it is generally not possible to find the correspondence of a single pixel in one image in a second image, once the gray value of a single pixel can be found at thousands of other pixels in the second image, and there is no unique correspondence. It is, therefore, considered finding the correspondence of a small neighborhood around the pixel of interest [25].

To solve the correspondence problem uniquely, the object surface has to exhibit certain properties. The ideal surface texture should, therefore, be isotropic, i.e., it should not have a preferred orientation. While it is relatively simple for a human observer to identify motion in successive images, it is not straightforward to formulate the problem in mathematical terms. In other words, motion estimation is not possible in regions of constant gray values.

3.1.5.1 Image Matching and Optimization Criteria

A simple method based on optical flow approach permits matching in varying lighting conditions and take object deformations into account. The Lucas–Kanade method is a widely used differential method for optical flow estimation developed by Bruce D. Lucas and Takeo Kanade [24]. It assumes that the flow is essentially constant in a local neighborhood of the pixel under consideration, and solves the basic optical flow equations for all the pixels in that neighborhood (see figure 3.7).

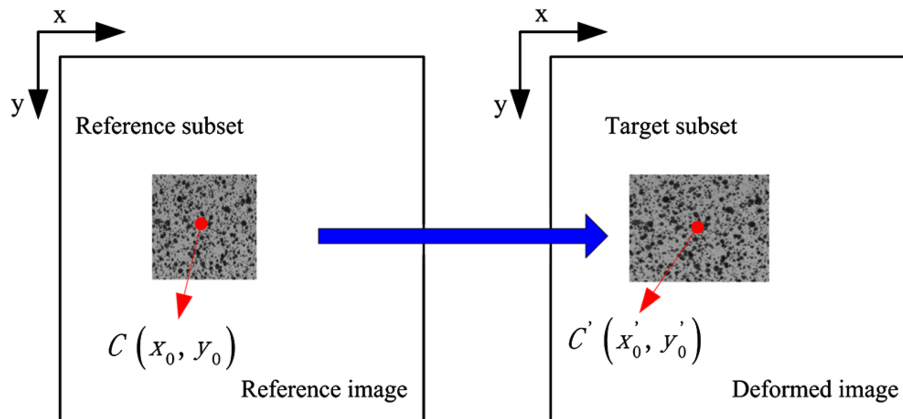

Figure 3.7: Digital Image Correlation determines a transformation that leads from one image $C(x_0, y_0)$ to another $C'(x_0', y_0')$. Adapted from [26].

Motion estimation method based on minimizing the gray value difference between a small subset from one image (template) and a displaced copy in another image. Even under near ideal experimental conditions, there will be differences between the intensity of two subsequent recorded images (changes in lighting, changes in specimen reflectivity due to strain or others).

The image correlation algorithm does not directly fit a displacement field to measured displacement data but accomplishes this goal through minimizing an error function defined on a secondary measure, the intensity distribution.

Considering it is known the reference image F and a target stressed image G and their associated gray values F_i and G_i, the optimization criteria that permits accurate template matching even if the images differ by an offset and a scale in lighting can be written as follow:

$$\chi^2_{ZNSSD} = \sum\left(\left(\frac{\sum \bar{F}_i\bar{G}_i}{\sum \bar{G}_i^2}G_i - \bar{G}\frac{\sum \bar{F}_i\bar{G}_i}{\sum \bar{G}_i^2}\right) - F_i + \bar{F}\right)^2 \tag{3.9}$$

The above equation is the so called zero-mean normalised sum of squared difference (ZNSSD) [25], where $\bar{F}_i = F_i - \bar{F}$ and $\bar{G}_i = G_i - \bar{G}$, being $\bar{F}$ and $\bar{G}$ the mean gray scale value.

Digital Image Correlation is typically used to compute a large number of displacement vectors throughout the image. The analysis is not limited to a single image, but rather applied to a sequence of images and the captured hundred images during deformation require the need to repeat the matching algorithm several million times.

The autonomous implementation of the DIC requires the obtaining of high-resolution images, using cameras coupled to an optical system with great magnification power. A typical image of cameras used in optical microscopy in $.TIF$ format is framed at 1280×720 pixels. Assuming focusing in a region of 10×10 mm^2, each displacement pixel represents a detection sensitivity of the order of 10 μm. By image correlation, it is possible to achieve sub-pixel resolution due to mathematical treatment, given the mentioned focus and the sub-pixel resolution (deformations of up to 10^{-5}, submicrometer accuracy) considering the whole focused region.

The application of DIC to the tensile device is still under study. Simulating in python language, the effectiveness of existing algorithms for artificial images are actually in order to validate the code before attempting to implement an image acquisition system coupled to the tensile device and integrated into the beamline.

3.2 DESCRIPTION OF SAMPLES AND EXPERIMENTAL TECHNIQUES

In this section, the synthesis of the sample used in the present work and the techniques used for their characterization is presented. The main samples of this work are composed of thin films deposited on deformable Kapton (polyimide) substrates. An important property that must be considered to act on the microstructure of thin films through the application of a macro-tension in the Kapton substrate is the adhesion between film and substrate. To this end, a thin layer of tantalum (Ta) is used as the *wettability* layer to impart adhesion between the film of interest (CoO) and Kapton. It proceeds, therefore, to the study of CoO / Ta / Kapton structures.

The morphology of the films is probed by atomic force microscopy while the deformations in the microstructure of the tensioned films are measured by the X-ray diffraction technique. The results serve to validate the concept adopted for the traction device.

3.2.1 Polymeric Substrate

In order to stress nanostructured films, it is necessary to support them on some flexible substrate, stretched in an elastic regime. The available options that are adequate to the require-

ments of elastic-flexible substrates are few, mainly related to polymeric materials. Among them, Kapton foils (polyimide film) are available in the LNLS and are widely employed in materials science research. The Kapton foils were developed in the 1960s by NASA and are suitable for use under extreme conditions of traction and temperature, besides being transparent to hard X-rays.

Existing in different thicknesses, Kapton foils proved to be a good initial choice because it was an easy-to-handle, extreme resistant material (stable at temperatures over 700 K and vacuum-compatible) with high Young's modulus (2.5 GPa), allowing a wide range of traction before the occurrence of plastic deformation.

The Kapton foils existing in the LNLS, however, has a visibly irregular surface (probably due to the factory method) for the different thicknesses existing. To assess the influence of the substrate on the films, an understanding of topological characteristics (roughness) of Kapton foil is necessary.

Initially, Kapton foils of 25, 50, 75 and 127 μm thickness were cleaned in order to eliminate possible organic contaminants using neutral detergent Merck 5% Extran MA02, iso-propanol bath at 373 K for 10 minutes and drying with dry N_2 and heating at 323 K. To check their temperature resistance, some samples were heated to 523 K using a plate for 30 min and compared to those duplicates not submitted to the same treatment.

The samples were then observed by light microscopy when the previous observations regarding the superficial irregularities were confirmed as well in the apparent no significant alteration with warming cases. All Kapton thicknesses studied have *bubbles* located below the surface plane and grooves supposedly due to the manufacturing process (see figure 3.8).

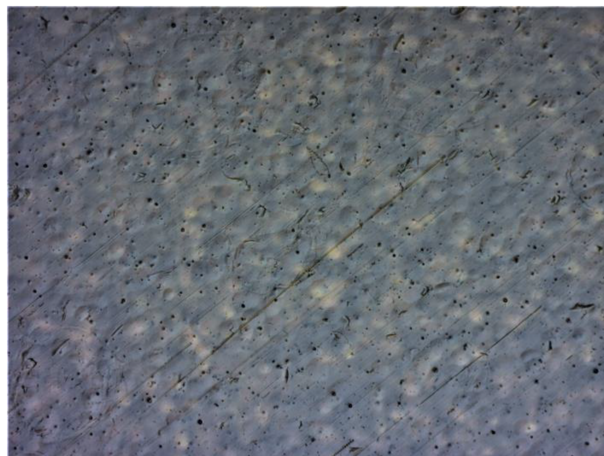

Figure 3.8: 50 μm Kapton substrate optical microscopy.

Considering the relationship between irregularity versus thickness and the fact that the substrate maintains its shape during traction, it was decided to use 50 and 75 μm sheets for the first deposition tests because they appear to be less rough (homogeneously distributed) after chemical cleaning. It is important to stress out here that for each foil several images were obtained, then assuring the homogeneity of the foils in terms of roughness.

3.2.2 Sputtering Deposition and Sample Description

To begin the study of antiferromagnetic films (AFM), a group of samples had been produced serving the investigation of obtaining textured CoO. The deposition of films was performed using the AJA Orion deposition system, which is part of the microfabrication group of LNNANO, a laboratory associated to CNPEM. The system uses targets 50 mm in diameter and up to 6 mm thick, and allows to simultaneously handle up to five different materials for deposition which generates possibilities to produce complex multilayer structures.

The desired CoO structure was prepared from *reactive sputtering*. Sputtering is a physical process based on the ion beam bombardment (inert gas ions - here Ar^+) of a target material of interest. The ions have enough energy to break down chemical bonding and eject atoms from the sample. The ejected atoms have a large mean free path on traveling from the target to the substrate. Given some optimizations, the sputtering process can produce layers of high quality and uniformity. It should be noted that the used tantalum (Ta) target was produced at CNPEM, machining to the necessary format and cleaning it chemically from a thin tantalum plate of high purity (99,98%).

In the *reactive sputtering* process the Co ions ejected from the target and adhered to the substrate (which is kept in the rotation to ensure homogeneity and reduce shadows effects, aiming for greater conformity to the deposition process) react with O_2 molecules inserted into the main deposition chamber to obtain the desired compound (CoO). The amount of O_2 inserted in the main chamber is controlled by their flow (usually measured in *sccm* indicating cm^3/min at a standard temperature and pressure) and this volume and will be the fundamental parameter used to control film stoichiometries. The total pressure (Ar plus O_2) is maintained at a certain amount keeping the plasma density required to deposition process occurrence. The deposition time is related to the thickness to be deposited (among other parameters) and must be calibrated to obtain the deposition rates. During deposition, depending on which process is being executed, may be interesting to heat the substrates: this can be achieved by halogen lamps heating a

metallic plate which heats the substrates by conduction.

In addition to Kapton substrates, samples were also deposited simultaneously on Si(111) and on Si(100), both with roughness previously determined to be of the order of an atomic step. The samples on Si(100) serve as a reference to characterize the growth process and to verify the structural quality of the deposited films, once Si has roughness of few angstroms, by this way do not transferring features (imperfections) to the subsequent layers. The Si(111) orientation shows a less flat surface and so is only used for deposition rate calibration.

In summary, 4 samples were prepared. The legend S_i (1 < i < 4) was adopted to describe different films grown on Si(100), Si(111), Kapton 50 μm, 75 μm, simultaneously. The deposition parameters are detailed below:

The first sample group (named sample 1 - S1) consists of a pure tantalum layer and has a purpose of calibration (by perfilometry). The Ta film aims at the formation of a transition layer (buffer) for adhesion (wettability) between the substrate and the cobalt oxide film of interest.

- Sample 1 (S1-K50, S1-K75, S1-Si100, S1-Si111): Tantalum film, deposition power of 100 W DC, Ar flow of 20 sccm, base pressure (Pb) of 5.4×10^{-7} Torr, deposition pressure (Pd) of 3 mTorr, for 30 min. Later profile analysis showed a 130 nm thickness (to be confirmed by X-ray analysis with better accuracy), higher than the 50 nm planned.

Sample 2 (S2) is formed only by CoO deposition by reactive sputtering and was used to calibrate the deposition rate. Due to variations in the amount of O_2 (fluxes of 1.0 and 0.5 sccm, suggested from preliminary studies) the stoichiometry of cobalt oxide can be controlled avoiding thus the formation of Co_3O_4 or other non-stoichiometric films (Co_xO_y).

- Sample 2 (S2-K50, S2-K75, S2-Si100, S2-Si111): Cobalt oxide (CoO*) film, deposition power of 150 W DC, Ar flow of 40 sccm, base pressure (Pb) of 6.0×10^{-7} Torr, deposition pressure (Pd) of 3 mTorr for 20 min. Later perfilometry showed a thickness of 100 nm (also to be confirmed by X-ray measurements), higher than planned.

For samples 3 (S3) and 4 (S4), the formation of CoO by reactive sputtering over a Ta layer was aimed. The deposition procedure adopted requires further annealing at 523 K for 5 min for both cases. It is needed in order to crystallize the system with the energy transferred.

- Sample 3 (S3-K50, S3-K75, S3-Si100, S3-Si111): CoO / Ta film, base pressure (Pb) of 7.0×10^{-7} Torr, deposition pressure (Pd) of 3 mTorr:

*nominal - stoichiometry is dependent of O_2 flow and can vary

- 1st layer (Ta): deposition power of 100 W DC, 40 sccm of Ar flow, 7 min, ambient temperature (298 K);
- 2nd layer (CoO*): deposition power of 150 W DC, Ar flow of 40 sccm and 0.5 sccm of O_2; initial 10 s Co deposition and subsequent O_2 injection, with total deposition time of 10 min; post-annealing at 523 K for 5 min.

• Sample 4 (S4-K50, S4-K75, S4-Si100, S4-Si111): CoO / Ta film, base pressure (Pb) of 8.0×10^{-8} Torr, deposition pressure (Pd) of 3 mTorr:

- 1st layer (Ta): deposition power of 100 W DC, 40 sccm of Ar flow, 10 min, ambient temperature (298 K);
- 2nd layer (CoO*): deposition power of 150 W DC, Ar flow of 40 sccm and 1.0 sccm of O_2; initial 10 s Co deposition and subsequent O_2 injection, with total deposition time of 10 min; post-annealing at 523 K for 5 min.

3.2.3 Scanning Probe Microscopy technique (SPM)

To confirm the initial perceptions and to improve the Kapton's surface properties understanding, Scanning Probe Microscopy (SPM) measurements should be performed. SPM technique was used to study morphology and to quantify the roughness of the used Kapton substrates and especially the films deposited on substrates of Si(100), whose was previously determined as being atomically flat (< 2 Å).

The SPM technique is a very high-resolution microscopy (nanometric to sub-nanometric resolution). The basic principle is to measure forces or interaction between a probe and the sample surface. The SPM imageability is based on the reaction of the probe to the imposed forces by the sample surface, used to form a high-resolution three-dimensional image of sample surface topography.

The SPM equipment consists of a cantilever with a sharp tip (probe) used to scan the specimen surface. When the tip is close to the sample surface, forces between the tip and the sample cause deflection on the cantilever. A laser beam is used to detect cantilever deflections towards or away from the surface. By reflecting an incident beam off the flat top of the cantilever, any cantilever deflection will cause slight changes in the direction of the reflected beam. A position-sensitive photodiode is used to track these changes (see figure 3.9).

*nominal - stoichiometry is dependent of O_2 flow and can vary

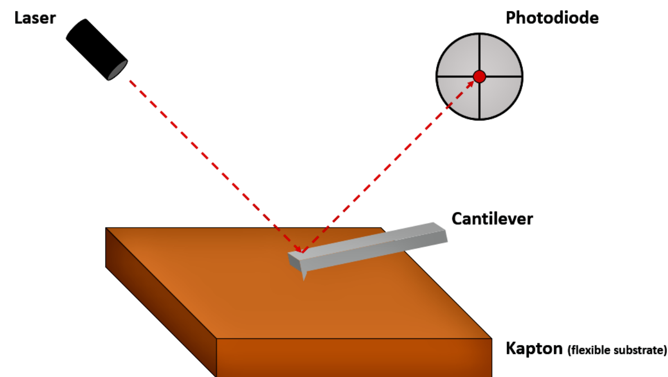

Figure 3.9: Schematic view of SPM analysis. Adapted from [27].

The topography information is achieved by scanning the sample and recording the height of the probe that corresponds to a constant probe-sample interaction (reached by using a feedback loop to control/monitor the height of the tip above the surface). Deviations of cantilever height represent the sample surface roughness.

The images were obtained using the NX10AFM equipment from Park Systems, located at the LNNANO (a CNPEM associated laboratory) microscopy center using the non-contact scanning mode.

3.2.4 X-ray Analysis Techniques

There are several characterization techniques that enable the elucidation of important structural properties. The use of X-ray scattering techniques for thin-film analysis is mainly motivated by two main reasons:

- The X-rays wavelength used is of the order of atomic distances, which qualifies their use as structural probes;
- X-ray scattering techniques are nondestructive.

3.2.4.1 X-ray Reflectivity - XRR

The electromagnetic waves incident on the sample are reflected in a specular direction. The total reflection occurs when the X-ray is incident on a flat surface of a material at a grazing angle smaller than the critical angle for total reflection (θ_c).

The main idea of XRR technique is to reflect an X-ray beam from a flat surface and to then measure the intensity of X-rays reflected in the specular direction. The intensity of the

reflected wave decreases rapidly with increasing the incident angle θ above θ_c [28].

XRR is sensitive to electron density change between adjacent layers being able to gauge films *thickness*, *density* and surface or interface *roughness* of the layers. The X-ray reflectivity method has the characteristic that it is applicable to the study of crystalline, polycrystalline or even amorphous films [28].

The reflectivity curve (see figure 3.10) has some characteristic features:

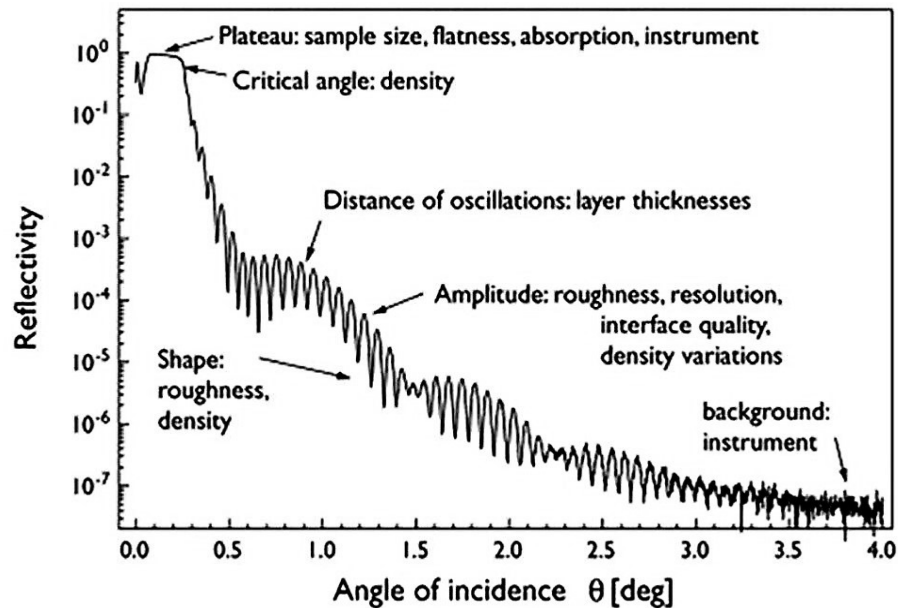

Figure 3.10: Template X-ray reflectivity curve. Adapted from [28].

- generally, the Y-axis of the reflectivity curve is shown in a logarithmic scale of the normalized intensity I/I_0. The logarithmic scale is used because of the wide dynamic range of X-ray reflectivity intensity;
- the reflectivity profile shows oscillations caused by X-ray interference between waves reflected from surfaces/interfaces. The oscillation depends on the film thickness, and the thicker film, the shorter period of the oscillations;
- the amplitude of the oscillation and the critical angle for total reflection provide information on the profile density of films;
- the reflected X-rays intensity decreases more rapidly with a larger surface/interface roughness (the larger the roughness of a film, the faster the decay rate of X-ray reflectivity intensity).

3.2.4.2 X-ray Diffraction - XRD

In addition to XRR studies, X-ray Diffraction (XRD) measurements were performed. Specifically, X-ray diffraction technique provides information of the crystalline phases existing as well a precise insight into the crystalline structure of materials, including possible deformations and preferential orientation of crystallites (texture). The physical principle is based on the constructive interference of the X-ray waves elastically scattered by the periodic atomic electronic density existing in (poly)crystalline materials [29].

Diffraction effects are observed when electromagnetic radiation impinges on periodic structures with geometrical variations on the order of the radiation wavelength [30]. X-ray waves interact with matter through the electrons contained in atoms, which are moving at speeds much slower than light. The scattering phenomena can be understood as follow: when the electromagnetic radiation reaches an electron (a charged particle), this electron becomes a secondary source of radiation (preserving energy and momentum), characterizing what is conventionally called *scattering the incident radiation*. The scattering of X-rays by atoms nuclei may be neglected. The X-ray scattering intensity can thus be modeled considering the number of Z electrons in an atom (electron density). When some atoms create a compound the electronic configuration is re-established and this new electron density is now responsible for scattering the incident radiation. Accordingly, constructive and destructive interference should become observable when crystalline and molecular structures are exposed to X-rays that are scattered coherently [29].

The diffraction condition can be mathematically expressed by the so-called *Bragg's Law* (see equation 3.10). This is a necessary but not sufficient condition to obtain a diffraction peak once not only geometric factors (right scattering angle) but also structural factors (as *atomic form factor* and *structure factor*) [31] play an important role in the diffraction event occurrence.

$$2d_{hkl}sen\left(\frac{2\theta}{2}\right) = n\lambda \tag{3.10}$$

where d_{hkl} is the interplanar distance and *hkl* is the Miller index associated to the crystalline planes. λ is the wavelength associated to the X-ray incident energy E by

$$E = h\nu = hc/\lambda \tag{3.11}$$

where h is the Planck's constant, ν is the radiation frequency and c the speed of light.

The wavelength λ is also related to the wave vector $\mathbf{K}$ by

$$|\mathbf{K}| = \frac{2\pi}{\lambda} \tag{3.12}$$

The Bragg's Law, therefore, allows to identify the crystalline phases and to determine the interplanar distances existing in the material. Moreover, it is possible to study the deformation existing in the crystal lattice.

A typical diffraction experimental setup is the so-called θ-2θ, where the diffracted intensity is measured as a function of the 2θ scattering angle while the sample is rotated by an angle θ. The diffraction event is an elastic scattering. In terms of the scattering vector (see figure 3.11) the mathematical condition is described by

$$|\mathbf{Q}| = |\mathbf{K} - \mathbf{K_0}| \tag{3.13}$$

where $\mathbf{K}$ is the wave vector of the scattered beam. The scattering vector $\mathbf{Q}$ is perpendicular to the surface of the film in the θ-2θ condition.

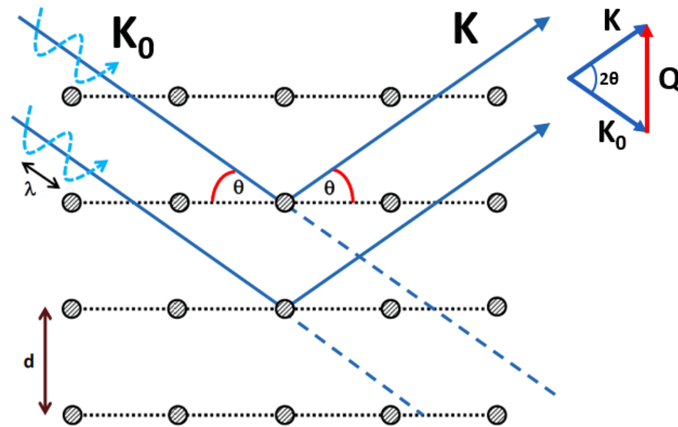

Figure 3.11: Definition of the scattering vector $\mathbf{Q}$ as a function of the incident wave vectors $\mathbf{K}_0$ and scattered $\mathbf{K}$. Adapted from [32].

Depending on how the sample is aligned relative to the incident X-ray beam, a distinct scattering vector is accounted by the detector. The most common diffraction experiment is based on probing those atomic plans that are aligned parallel to the film surface (see fig 3.12). At this geometry, it is usual to name the scattering vector $\mathbf{Q}$ as $\mathbf{q}_z$ once it points out at the same direction of the normal surface vector (see figure 3.13a).

For the case of polycrystalline thin films (see figure 3.12), the θ-2θ measurement is sensitive only to those crystallites whose atomic planes are parallel to the surface.

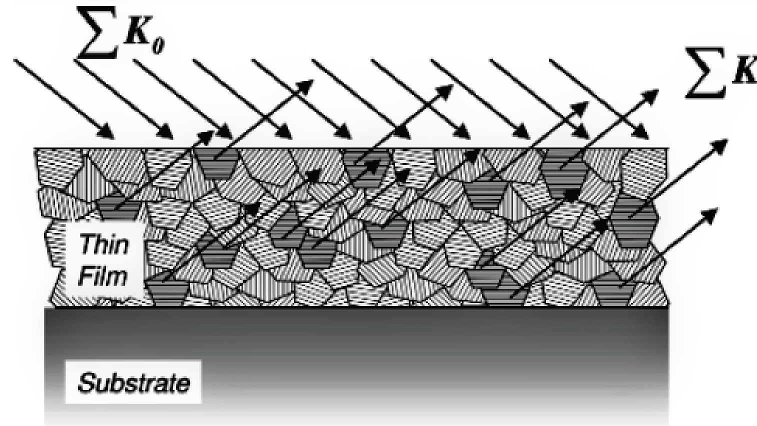

Figure 3.12: Measurement θ-2θ of thin films probe flat crystals orientated along the surface. Adapted from [30].

However, it is also possible to obtain structural information of the atomic plans arranged perpendicularly to the film surface. Rotating correctly the sample over the imaginary scattering plane formed by the incident beam and the detector, scattering events from plans aligned at x ($\mathbf{q}_x$ scattering component) and y ($\mathbf{q}_y$ scattering component) are recorded by the detector (see figure 3.13b and 3.13c).

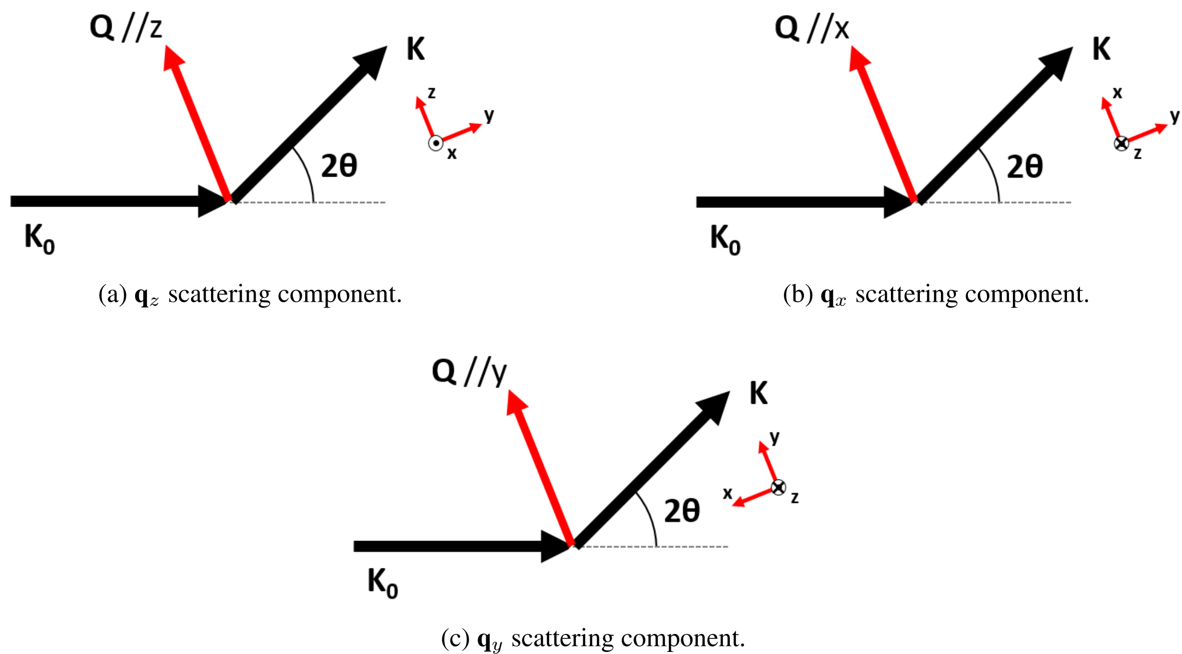

(a) $\mathbf{q}_z$ scattering component.

(b) $\mathbf{q}_x$ scattering component.

(c) $\mathbf{q}_y$ scattering component.

Figure 3.13: Due the relative alignment of the sample to the detector, distinct scattering components from different crystallites orientations are being probed.

During the synthesis process, the thin films usually suffer from the occurrence of *mechanical stresses*, which are mainly introduced by a specific process or a post-treatment. It is named *residual stresses* and in most of the cases it is caused during the deposition process. In

the case where the stresses are measured during loading they are named *load stresses* [30].

The films produced by sputtering technique show, naturally, residual stress. The main goal of the tensile device is to probe the sample with synchrotron light while it is subjected to a biaxial tensile stress state at progressively higher applied load. The XRD measurement involves measuring interatomic distances compressions of a crystalline phase existing at the sample and so measure lattice parameter changes *in-plane* and *out-of-plane* directions.

Moreover, the correlation between lattice strains and macroscopic strains measured is an important information concerning the elastic deformation and grains interaction. Hence, the tensile device has to be designed such that precise measurement of macroscopic strain be possible.

4 RESULTS AND DISCUSSIONS

Once it was stipulated the requirements and constraints of the tensile device needed to perform the proposed XRD experiments, it was time to develop and design the device. After a learning stage, it was possible to build up the first prototype of the device that is now presented. Even considering that a second version of the device should be constructed, this first prototype presented some of the basic requirements needed from the experimental point of view. The second version was already projected, as demonstrated in this section.

Throughout this section it will be discussed features of samples, X-ray techniques measurements and further results achieved that validates the ideas proposed to be executed.

4.1 FLEXURE DEVICE

A first approach to validate the use of flexure concept as a linear guide, a prototype adapted from an already available system at LNLS, was used allowing to perform diffraction experiments in thin films with *in situ* stress condition at XRD2 beamline.

The prototype was adapted from a *bending silicon monochromator sagittal crystal* system whose installation on the XPD (X-ray Powder Diffraction) beamline was unsuccessfully attempted by the middle of the 2000s. This device is equipped with two linear actuators (stepper motors with power screws), with axial force up to 90 N (model Faulhaber AM1524, with a 76:1 gearbox), positioned antiparallel. Each actuator acts on a mobile platform that rotates guided by flexures structures. This device, which was idle, was mechanically adapted and its engines integrated into the XRD2 beamline control system. Clamps were manufactured to fix the polymer sheets to the device frame (see figure 4.1).

This prototype adapted is not entirely adequate for the intended purpose: it performs a rotational movement, what in practice means changing sample height, requesting, therefore, successive realignments during the diffraction experiments. However, this same device allows testing the calculated/manufactured clamps and their abilities fixating Kapton sheets, testing the concept of flexure guides for uniaxial traction and, observing the necessary correction at the sample height when performing diffraction experiments on tensioned films.

The specific biaxial tensile device which only executes the translational movement was designed considering technical aspects related to the materials choice and machining procedure: the device is *mountable* machine, and thus their manufacturing process is facilitated.

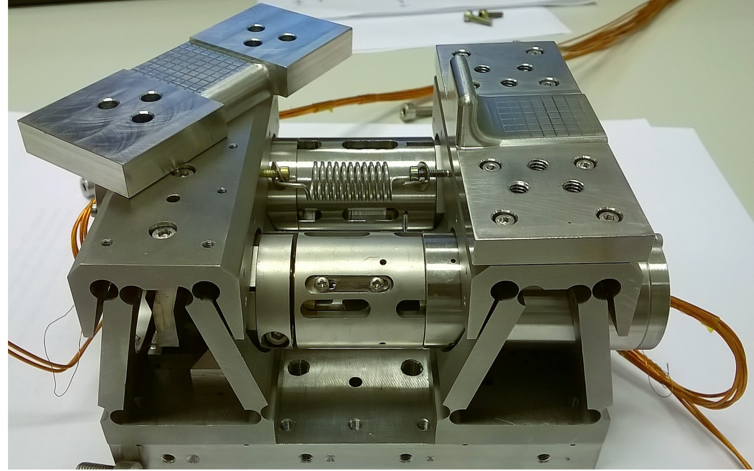

Figure 4.1: Bending silicon monochromator sagittal crystal system (in disuse). Silicon crystal bracket has been replaced by the clamps; Kapton's rectangular sheet is stretched guided by a rotational movement performed by the system around a virtual plane (designing feature), changing thus the height of sample position.

An important consideration is the material choice to flexure device machining: as mentioned, the device is composed of small amounts that, when bringing it together, executes exclusively the proposed translational motion with the desired precision. However, each constituent has its own functionality and therefore different material properties are required. The considered materials to flexure component itself must have high Elastic Modulus, or tensile modulus, to avoid deformation and so fatigue, and low thermal expansion coefficient (preserving the projected dimensions); the thermal diffusivity parameter is not critical since the machine is going to work at normal ambient conditions. The tensile device is still at conceptual period (not machined), but the material that better fits the required features is the Stavax, a *premium* stainless, density (ρ) of 7.8 g/cm^3 at 20°C, modulus of elasticity 200 GPa and tensile strength (the capacity of a material to withstand loads tending to elongate) of 1780 MPa, with negligible thermal expansion at room temperature [33].

Other components (as linear actuators support, power screws, clamps and further) will probably be machined on stainless steel. Considering the imposed constraints, all components were dimensioned and arranged in such a way to respect weight and size. In this way, however, stainless steel may not be the best choice since it is dense (around 8.0 g/cm^3): the mentioned components, therefore, would represent substantial amount on tensile device total weight. Here the relation between density (weight) and stiffness (how much it resists deformation in response to an applied force) is crucial to the success of the tensile device project. This parts probably are going to be machined using aluminium (density around 2.7 g/cm^3).

As accomplished to bender adaptation, the system axial load capacity to the XRD2

beamline device was dimensioned. The force range (above to 200 N to each traction direction) is being stimulated to be higher to that existed on the adapted bender flexure system (to creates larger stretching possibilities), and so the power screws must be dimensioned aiming to sustain higher reaction force (achieved by its smaller thread pitch). The stepper motors do not need to respect special work conditions; also the coupled gearhead do not require any special specification. It is desirable, however, that it has a high reduction ratio to precision motion: it is being planned to use a *planetary gearhead* with a reduction ratio of 592:1 and a maximum axial supported load of 30 N, also from Faulhaber Motors. Beyond to reduction ratio, the gearhead should be as small and light as possible, and so others possibilities are under investigation. To the final design, nevertheless, this uncertainty do not imply project changes: the gearhead diameter size from Faulhaber company is standardized.

The design of the flexure-based device to XRD2 beamline sample environment consists of 2 leaf springs in parallel, which are used as a (quasi-) linear guidance. Through a double parallel leaf spring (in series), parasitic displacements can be eliminated (see figures 3.4 and 3.5). Besides, by simple relationships, it is possible to reinforce all structure, respecting, however, the projected stiffness (C) along all directions (x, y and z). This *good practice* concept facilitates machinability and assures higher life cycle to the device.

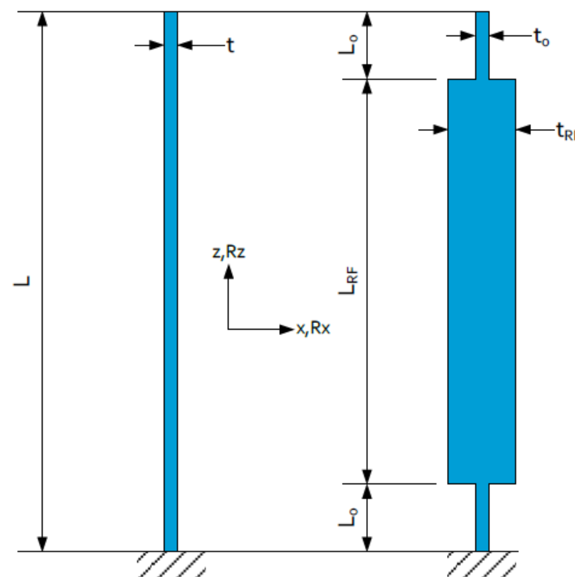

Figure 4.2: Reinforced leaf spring: the bending movement is fully realized by the thin parts. The reinforced part is assumed to be infinitely stiff, without suffering any change during bending. Adapted from [34].

The following figures (see figure 4.3 and 4.4) shows the last design version. The machine is being lovely called **TeDi** (acronym to Tensile Device).

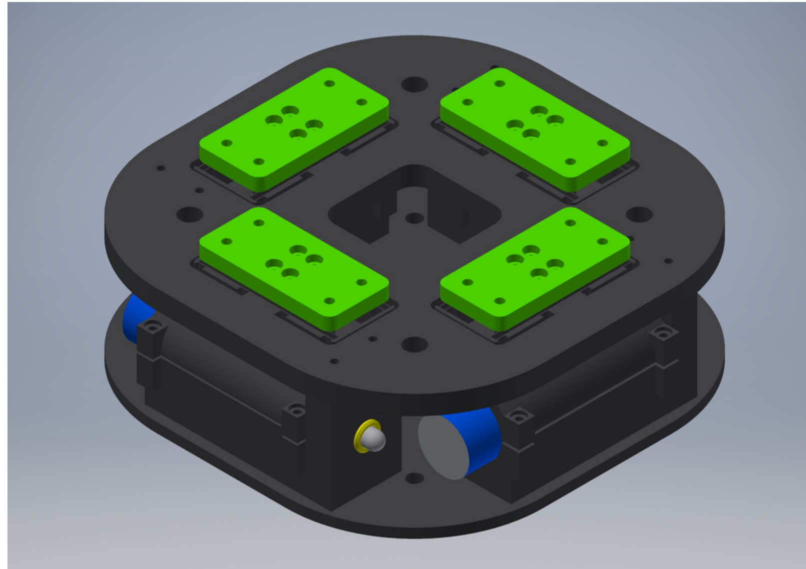

Figure 4.3: TeDi last design version: it still requires verification of some details but it will be machined soon.

As can be seen in figure 4.4a, the upper frame (which contains the flexure structure) is also separable, facilitating its machining. Figure 4.4b shows clamps which were rescaled from those of the first test. Figure4.4c and figure 4.4d show the stepper motors (linear actuator), the support frame and necessary sub-components to force system operation.

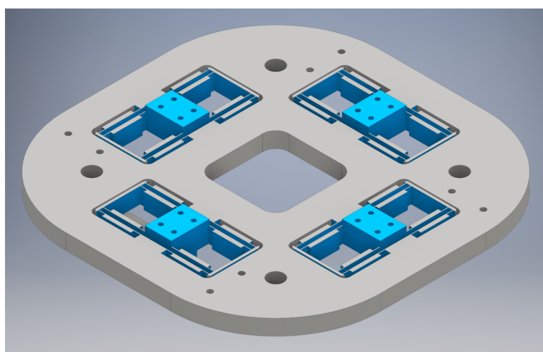

(a)

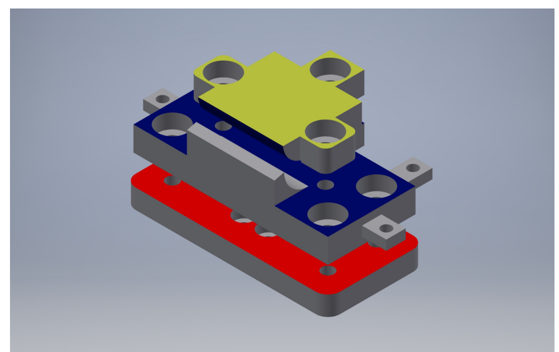

(b)

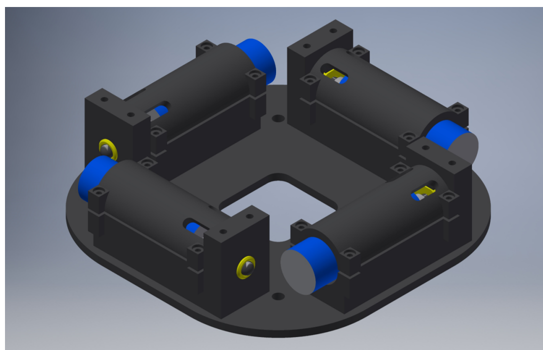

(c)

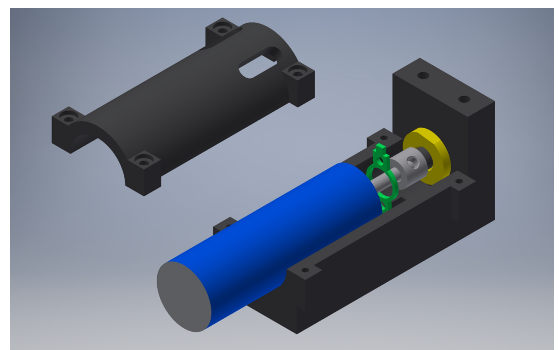

(d)

Figure 4.4: TeDi is a partitioned machine.

4.2 FINITE ELEMENT ANALYSIS

One of the most challenging aspects of the biaxial testing setup is the specimen design once the center of the substrate specimen must exhibit a homogeneous strain area larger than the irradiated X-ray area.

The 2D FEA were performed using a toolbox of *partial differential equations* from the Matlab2016a environment. The simulation was focused on the study of cruciform Kapton substrates in which the arms' length, width and the radius of the junction between the arms was varied to test its shear rupture limit (which it is critical as long the radius is reduced) and the load distribution of the central deformed region (homogeneity worsens with larger radius), creating then an engagement between strain homogeneity and Kapton deformation.

As already explained about FEA (read section 3.1.4), the 2D simulation requests some material properties to calculate deformations fields:

- Young's Modulus (E), also known as the elastic modulus, is a measure of the stiffness of a solid material. The Kapton Young's Modulus value is 2.5 GPa;
- Other important parameters from Kapton are density (1.42 g/cm^3) and Poisson's ratio (0.34);
- Another important feature is the yield point (yield strength), a material property defined as the stress (σ) at which a material begins to deform plastically, around 70 MPa to Kapton. Here, however, it is dealt with substrates at their plastic regime;
- For the simulation with Kapton, two thickness (t) (50 μm and 75 μm) and two widths (w) (between 10 mm and 15 mm) were studied. The aimed deformation ($\epsilon = \Delta$L/L$_0$) of about 3% is related to a stress of 70 MPa, approximately. This value arises from Hooke's Law applied to materials;

$$\sigma = E\,\epsilon \tag{4.1}$$

- By knowing the applied stress it is possible to determine the force (F) applied over a cross sectional area (A) which corresponds to the desired strain (equation 4.1) and that must be added as boundary condition to simulation.

$$\sigma = \frac{F}{A} \tag{4.2}$$

Figure 4.5 shows the strained field simulation of a 75 μm thick cruciform Kapton with arms 15 mm width and 50 mm length and 3 mm junction radius, submitted to a traction of 50 N

at both x and y directions. The described scenario means the extreme situation that the Kapton foil will be submitted.

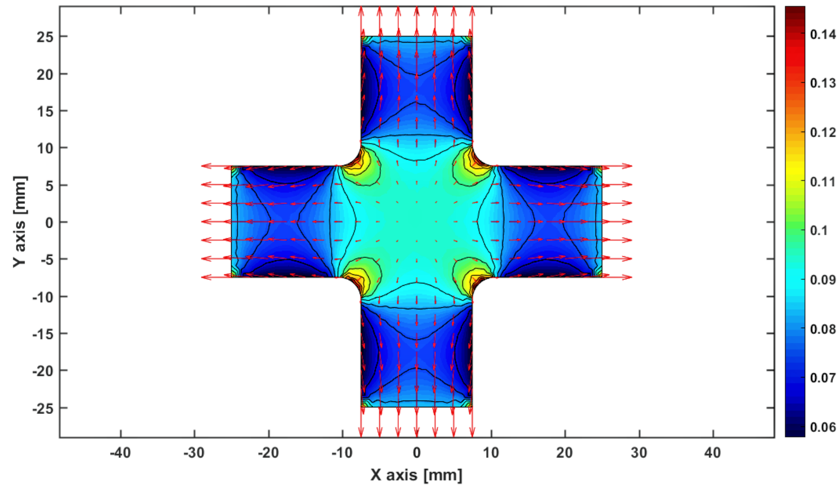

Figure 4.5: Deformation field (color scale in mm) of 2D substrate; arrows indicate the displacement on different regions.

From the simulated format in figure 4.5, it is possible to verify a radial variance relative to the central region lower than 10^{-2}. The homogeneous load distribution is lost by shear effect taking place, critical for higher tensile conditions. This condition appears due to the radius purposely built between arms. However, it is impossible to create a perfect sharp 90° cut during substrate preparation and so it is better to control the "error" on the shape and therefore, knowing the source from the non-homogeneous condition.

Even with the occurrence of an undesirable stress, it should be noted that the typical beam size at LNLS beamlines is of few mm^2 (XRD2 has a beam size of 0.5×1.5 mm^2 FWHM at 8 keV, the vertical and horizontal focus at the sample). From simulated substrate, the homogeneous load distribution area is of 8×8 mm^2, at least.

As just mentioned, the beam size is smaller than the simulated region of interest. However, the cruciform specimen are 10 mm width: substrates will be chemically cleaned and it is hard to handle them in case they are too small.

Given the result of this simulation, Kapton sheets will be cut in the simulated format for later deposition of the films. In order to limit the deposition of the films of interest to this region of great homogeneity, a mask (on steel - 1 mm thick) with a central circular hole (12.5 mm in diameter) was produced and it will be used for further depositions.

4.3 SCANNING PROBE MICROSCOPY MEASUREMENTS

The performed SPM measurements aimed to obtain information with a nanometric resolution about the morphology of films. This study is relevant to the understanding of the growth mechanism of the samples allowing identifying, for example, the existence of large homogeneous regions or the formation of agglomerates, depending on the deposition parameters.

In addition, to observing Kapton foils chemically cleaned, the samples deposited on Kapton and Si(100) substrates were also measured, with the main focus for the samples on Si(100) (avoiding have contributions from substrate roughness).

As already mentioned, Kapton samples are rough (σ of 10 nm RA), with few terraces and furrows (grooves) with preferential direction, given the lamination suffered during manufacture process (see figure 4.6).

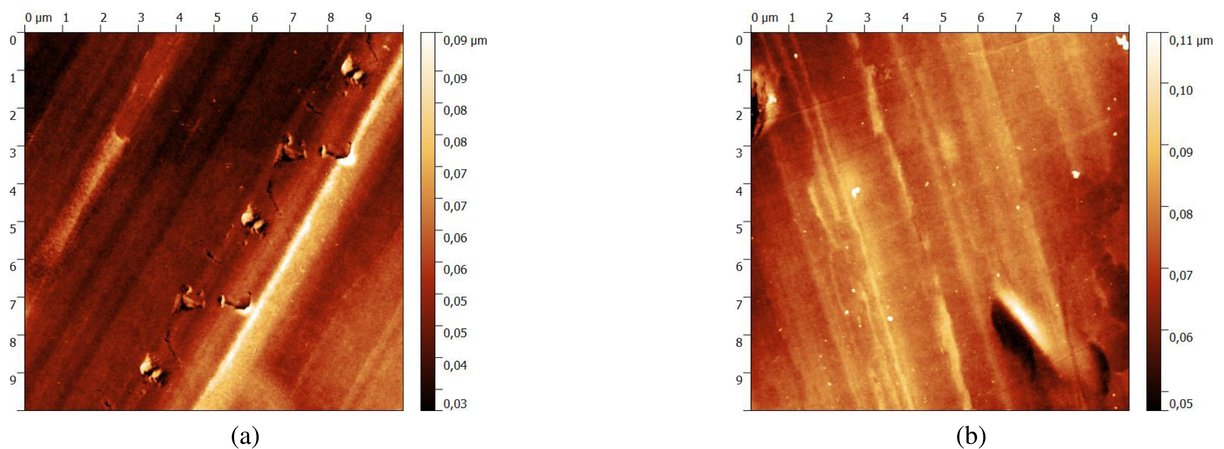

(a) (b)

Figure 4.6: Kapton substrate 50 μm (right) and 75 μm thick (left) (10×10 μm^2).

The SPM measurements of the thin films deposited on Si(100) provide hints on the growth process of the films of interest. For samples S1 (Ta / Si) (figure 4.7a), the roughness σ_{S1} of 0.5 nm RA (an arithmetic average over all scanned area - 10×10 μm^2) remains close to that observed for the clean substrate, even for a film of approximately 130 nm. This result confirms that, from the morphological point of view, Ta is a suitable material for using as buffer layer or wettability.

The samples S2 (CoO / Si) and S3 (CoO / Ta / Si) (figure 4.7b, 4.7c) show a slight increase in roughness (σ_{S2} of 1.5 nm RA and σ_{S3} equal to 0.6 nm RA). This roughness is surprisingly small for CoO films since even in ultrafine layers (< 10 nm), this oxide tends to form rough surfaces [10]. This observation is an indication of the insufficiency of O_2 in the deposition chamber during the reactive sputtering (to be confirmed with XRR analysis).

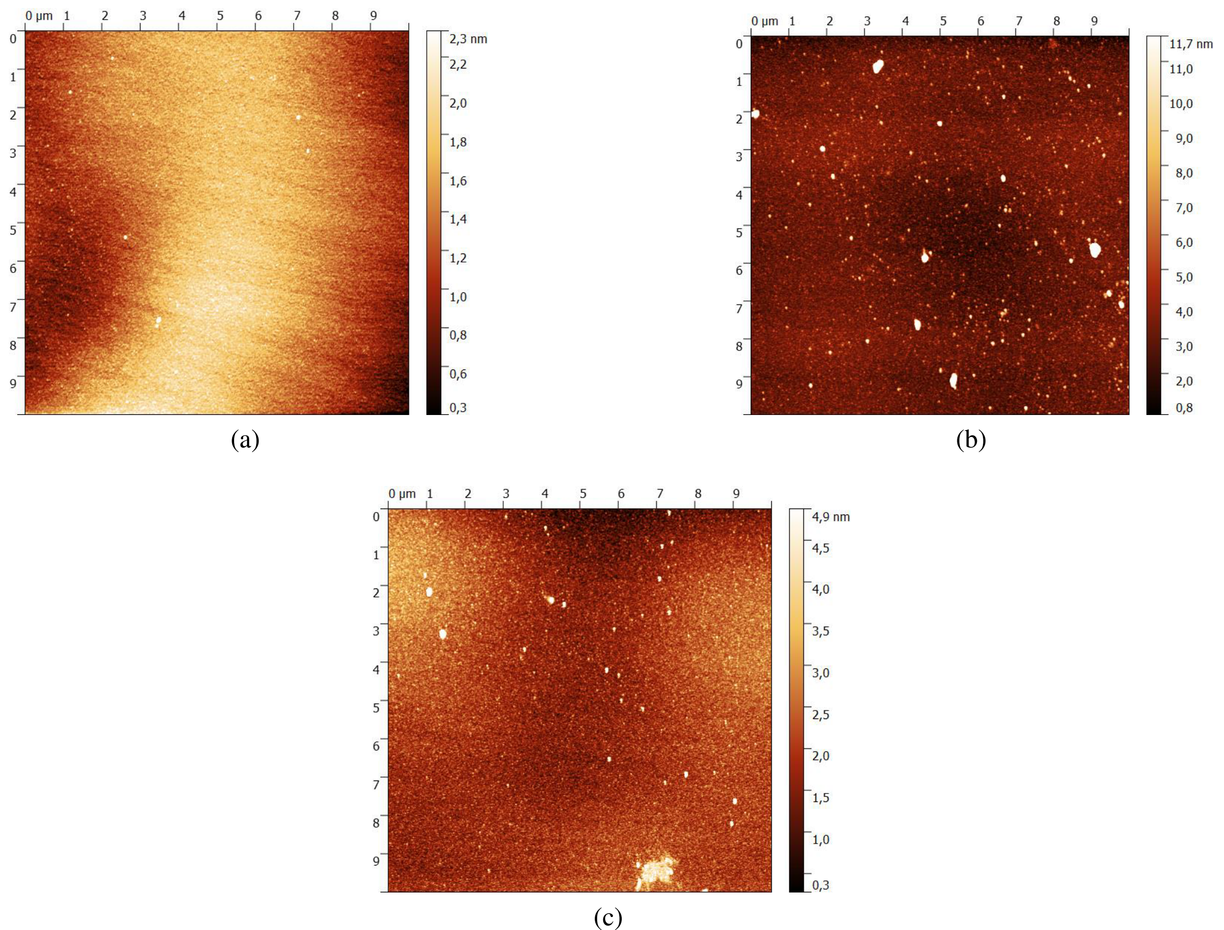

Figure 4.7: SPM images of films deposited on Si(100) substrate (S1, S2 and S3, respectively).

4.4 XRD and XRR MEASUREMENTS

The films deposited on Si(100) were structurally characterized by XRD and XRR measurements during beamtime at XRD2 beamline. The thin films on Kapton under mechanical traction were also studied. As will be discussed later, only the sample S1, which presented a well-defined crystalline phase, allowed testing the traction of thin films. Samples S2, S3, and S4 did not present the desired CoO crystalline phase. However, the XRR measurements provide information of layers density from which we can infer about the obtained stoichiometries.

From X-ray reflectivity, it is possible to determine the layer thickness (t), roughness (σ) and density (ρ), currently the most important parameter from the produced samples. The use of the IMD package, an extension to the free XOP 2.4 software [35], allows the simulation of the XRR reflectogram.

Usually, cobalt oxide (CoO) presents a density around 6.44 g/cm^3 (or lower due to sputtering deposition process). The simulation of XRR measurement, however, shows a density around 7.6 g/cm^3, related with non-stoichiometric $\mathrm{Co}_x\mathrm{O}_y$ (Co/O ratio > 1) or even metallic

Co formation (cobalt density is around 8.90 g/cm^3). The low roughness (less than 5 nm) also corroborates with the non-oxidation of cobalt. Simulated thickness, however, is very close to 100 nm, as it was estimated from perfilometry. This result verifies the need to adjust parameters for future depositions. As expected from the SPM images, by XRR measurements (see figure 4.8) it was possible to confirm that there was oxygen insufficiency during deposition.

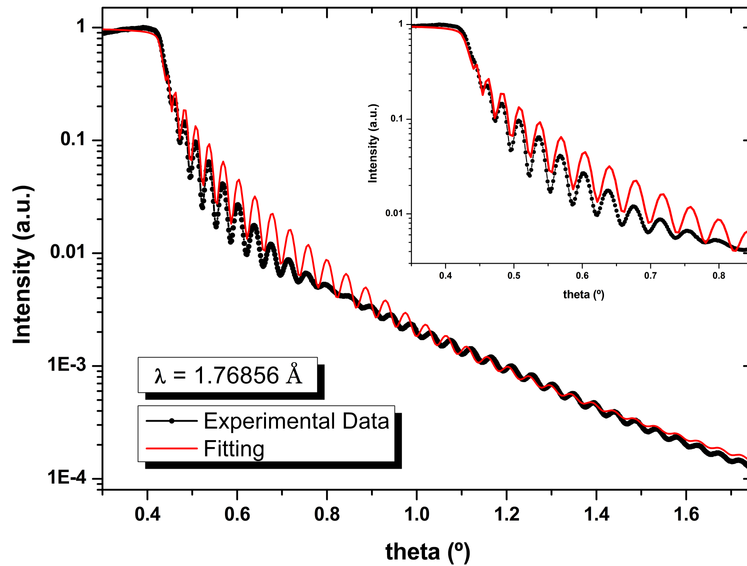

Figure 4.8: The simulation of XRR from sample S2 (CoO* /Si) showing higher density than suspected; probable metallic Co occurrence.

Even with the non-fully complete fit, from it is possible to conclude about the thickness (oscillations period) and density (related to the critical angle), both well adjusted.

Relative to the stress study, initially the movement of the flexure device was characterized. Due to the rotational movement of the flexure, the displacement in the sample position (cheek surface) is not even performed by the actuators. The calibration of the correspondence between the movement of the actuators against the movement of the sample was characterized by the use of a *caliper rule*.

Due to the rotational movement of the flexure prototype, the height of the sample changes after increase (or decrease) stress, and so it must be corrected (alignment is crucial on diffraction experiment, especially when dealing with polycrystalline thin films). According to this, a calibration curve was obtained which relates the sample height (X-axis of the diffractometer) for each traction stage.

The flexure device was adapted to the diffractometer (see figure 4.9) and its control integrated to the beamline system.

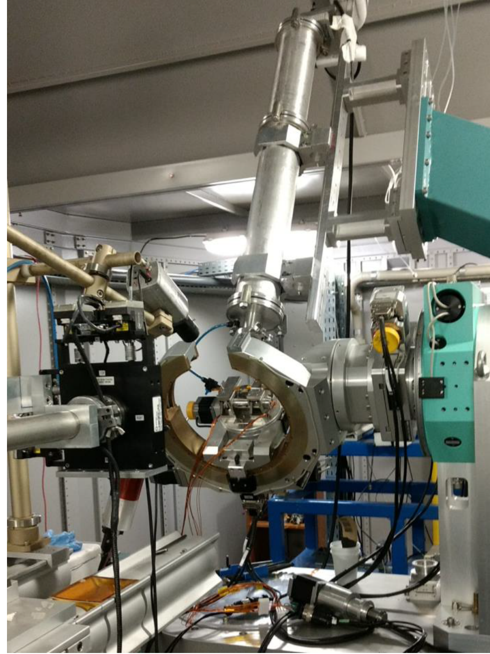

Figure 4.9: Usual θ-2θ ($\mathbf{q_z}$ scattering) experimental setup at XRD2 beamline.

Figure 4.10 shows a diffraction measurement θ-2θ of sample S1 (Ta on Si(100)). It is possible to observe only 3 diffraction peaks, two of them being narrow and intense are identified as the (002) Bragg reflection and its harmonic (004) of the tetragonal tantalum β phase. The third peak corresponds to a diffuse scattering from the peak (004) of the Si(100) substrate (misaligned). This observation indicates that the Ta film grows with a strong texture [001], since only this family of atomic plans was checked and that the measurement in the θ-2θ geometry probes the atomic planes aligned parallel to the surface of the substrate (see figure 3.12).

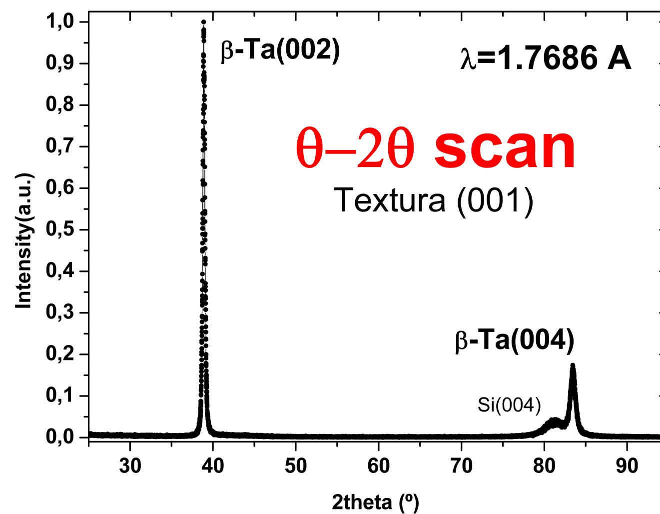

Figure 4.10: θ-2θ diffraction measurement of S1-Si100 sample (Ta / Si). Crystallization takes place in the β phase, presenting texturization [001].

Given the observed [001] texture, it is expected that the diffraction peaks coming from atomic planes perpendicular to this direction will be observed by rotating 90º the sample (*chi* axis in the 6+2 circle diffractometer of XRD2 beamline, see fig. 4.11) so that the scattering vector is parallel to the surface of the film. This is the β-Ta(410) reflection, which was effectively observed when positioning the sample and the detector at the corresponding angles, confirming the observed texture. In the films deposited on Kapton substrate, the same behavior is verified. Then, these samples were used to verify the validity of traction model by observing the displacement of the Bragg peaks as a function of the films traction.

A useful way to understand the diffraction experiment relative to the stress direction and film texture is to define the sample reference as follows: the **z-direction** is perpendicular to the film, **x** is parallel to the film and to the traction direction and **y** is parallel to the film and perpendicular to the traction. From this definition, θ-2θ measurement means **Q** // $\mathbf{q}_z$, while measuring after rotating a diffractometer stage (*chi* stage) by 90º, **Q** // $\mathbf{q}_x$ (see figure 4.11). At the present case, to measure $\mathbf{q}_y$ scattering component (which is not possible in this version of the device by shading effect) it would be necessary, from the measure of $\mathbf{q}_x$, to rotate the sample azimuth angle (*phi* stage of diffractometer) by 90º.

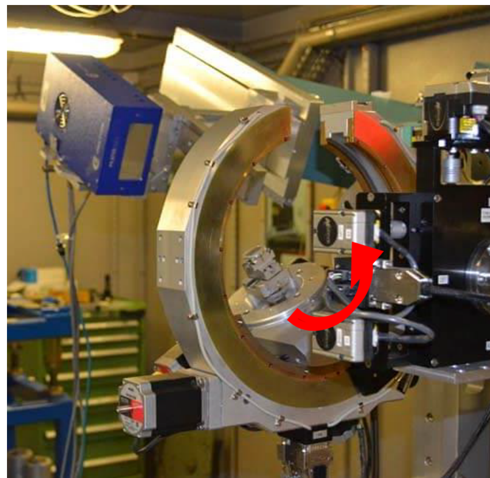

Figure 4.11: Representative $\mathbf{Q_x}$ scattering setup at XRD2 beamline.

Figure 4.12 and figure 4.13 show diffractograms of the (002) and (410) Bragg reflections of the β-Ta phase (**Q** // $\mathbf{q}_z$ and **Q** // $\mathbf{q}_x$ respectively), as a function of the traction applied along the x-direction. It is possible to observe the relative displacement of the Bragg peaks, corresponding to the variation of the interplanar distances d_{hkl} resulting from the applied traction. In the z direction, Bragg reflection (002) move toward larger angles (*decrease* of the interplanar distances).

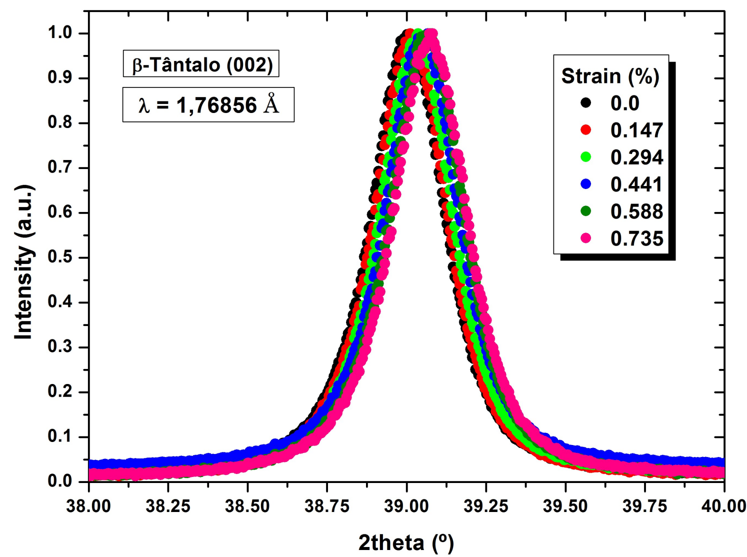

Figure 4.12: Decrease in interplanar distance (decrease of lattice parameter **out-of-plane**) with increasing stress $(1/d_{hkl}^2 \sim 1/c^2)$.

In turn, in the x-direction (orthogonal direction), the inverse occurs: Bragg reflection (410) moving toward smaller scattering angles, indicating a microstructure distension (*increase* of the interplanar distances), as expected from the traction direction.

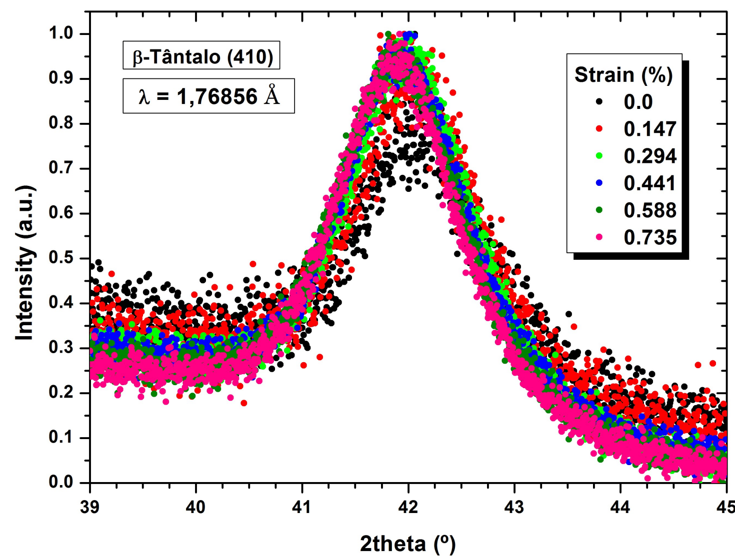

Figure 4.13: Increased interplanar distance (increase lattice parameter **in-plane**) with increasing stress $(1/d_{hkl}^2 \sim 1/a^2)$.

These displacements observations occurring with the Kapton foil in the elastic regime allow checking the adherence of the Ta film to Kapton, indicating tension transmission from substrate to the deposited CoO film. The film was stretched to the limit available on the device (plastically stretching the Kapton).

The obtained interplanar distances as a function of Kapton deformation are summarized in figure 4.14 and figure 4.15. As can be seen, tantalum film undergoes a microstructural rupture from a Kapton deformation of approximately 0.75%.

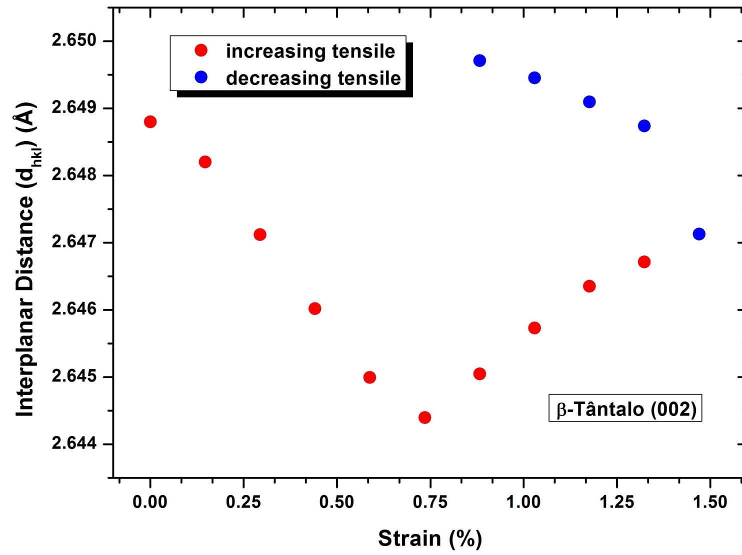

Figure 4.14: Measurement of the scattering component $\mathbf{Q}$ out-of-plane $\mathbf{q}_z$; decrease of the interplanar distance when increasing the applied stress.

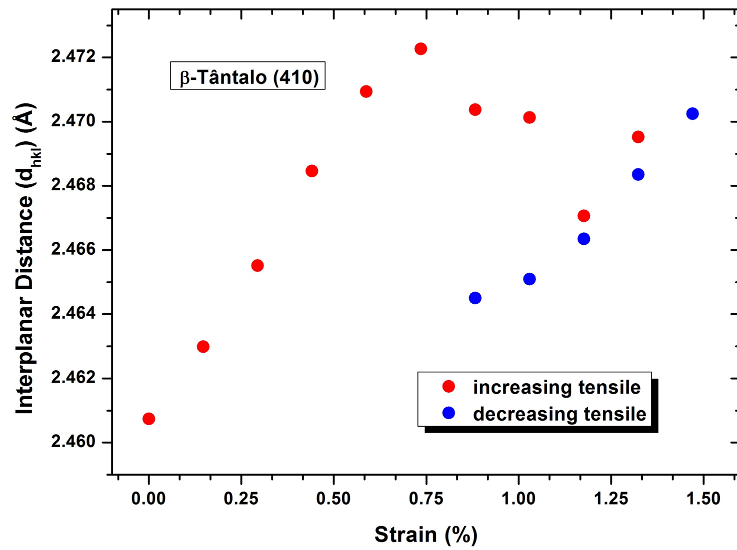

Figure 4.15: Measurement of the scattering component $\mathbf{Q}$ in-plane $\mathbf{q}_x$; increase of the interplanar distance when increasing the applied stress.

The interplanar distances shown in the two curves above were obtained using the Bragg's Law by adjusting the position of the diffraction peaks by a Gaussian function. The uncertainty in the adjustment performed (at angle 2θ) was always less than 10^{-4} degrees, which translates into a corresponding uncertainty in d_{hkl} of less than 10^{-4} Å as well.

5 CONCLUSIONS

One of the current projects existing in the XRD2 beamline at Brazilian Synchrotron facility is to study thin films through plastic deformations in the crystalline structure of AFM materials, especially CoO. For this purpose, an instrument of tension was planned.

It was desired to obtain a formula for the AFM samples deposition with high structural quality and a high degree of texture (presenting a preferential orientation of crystallographic planes). The first depositions showed the need of adjustments: the O_2 flow adopted as well the selected power used in the Co sputtering, aiming CoO formation, inhibiting phases such as Co_3O_4 and/or Co_xO_y. On the other hand, initially, there is no evidence of problems with film adhesion when deposited on elastic/flexible substrates.

The mechanical concept adopted (use of flexure structures) was adequate. Tests using an adapted (not optimized) device were very promising, generating relevant aspects that support the initiative in investing on the design of a mechanical device based on compliant mechanisms. The aforementioned effort, much more than being used only in the design of the XRD2 prototype, is justifiable to generate knowledge to future developments to SIRIUS, being timely in view of the imminent need for greater stability and mechanical precision required in the new accelerator, favored through the use of flexures.

The finite element simulations proposed for the understanding of the load transference between device and substrate indicate that for different proposed formats, to be tested over a wide range of forces, the homogeneous charge distribution region is larger than the beam size existing at the XRD2 beamline of LNLS.

Aside from the mechanical concept, the use of digital image correlation (DIC) for *in situ* strain determination is not yet implemented. It has short response time (few milliseconds) and high accuracy (already achievable in simulations), but still requires the hardware implementation with the definition of the image acquisition system.

About XRD analysis, the obtained diffraction patterns allowing to measure interplanar distances (d_{hkl}) and to verify the load transfer model between the film and the polymeric substrate behaves as proposed.

6 PERSPECTIVES

The development of the biaxial tensile device requested time, patience, and effort on technical specifications elaboration. There was also a time to *self convincing* and certification that the most suitable concepts were being correctly applied and therefore, those project expenditures (personnel and resources) would being justified.

After studying the scientific aspects (flexure based devices, FEA, DIC, antiferromagnetic theory, diffraction, etc.) and therefore attest the approach to be taken next, the project began to be planned, involving a large number of people, each of them with its qualities and experience.

It has already been shown the partial success and the obtained results motivate the sequence of work to further understanding. To continuous improvement and fully prosperity, there are some perspectives of the work:

- The flexure hinge concept, which initially looked to be indecipherable and therefore challenging, was at least conceptually developed. The machining is being planned to occur as soon as possible to be available yet for the first semester of 2017;
- As mentioned, the Digital Image Correlation implementation did not have too many advances. Its implementation is a priority from now on as it is the most reliable method to certify about thin films deformation;
- New samples must be prepared, now with improved sputtering parameters; the thin films would be first tested on a common diffractometer and the synchrotron light held to further and detailed understanding.

After the mentioned improvements, besides XRD2, other beamlines must test and attest the biaxial tensile device (TeDi).

REFERENCES

[1] Richard P Feynman. There's plenty of room at the bottom. *Engineering and Science*, 23(5):22–36, 1960.

[2] Norio Taniguchi et al. On the Basic Concept of Nanotechnology. In *Japan Society of Precision Engineering*, pages 18–23, 1974.

[3] Philip Willmott. *An Introduction to Synchrotron Radiation: Techniques and Applications*. John Wiley & Sons, 2011.

[4] Guillaume Geandier et al. Development of a synchrotron biaxial tensile device for in situ characterization of thin films mechanical response. *Review of Scientific Instruments*, 81(10):103903, 2010.

[5] Tomas Jungwirth et al. Demonstration of molecular beam epitaxy and a semiconducting band structure for I-Mn-V compounds. *Physical Review B*, 83(3):035321, 2011.

[6] Fabio Pulizzi. Spintronics. *Nature Materials*, 11(5):367–367, 2012.

[7] Tomas Jungwirth et al. Antiferromagnetic Spintronics. *Nature Nanotechnology*, 11(3):231–241, 2016.

[8] P Bodeker et al. Spin-density waves and reorientation effects in thin epitaxial Cr films covered with ferromagnetic and paramagnetic layers. *Physical Review B*, 59(14):9408, 1999.

[9] BG Park et al. A spin-valve-like magnetoresistance of an antiferromagnet-based tunnel junction. *Nature Materials*, 10(5):347–351, 2011.

[10] Anne Lamirand. *Croissance épitaxiale, structure atomique et couplage d'échange de bi-couches ultra-minces d'oxydes sur métaux*. PhD thesis, Université de Grenoble, 2014.

[11] WebElements, Cobalt Oxide. https://www.webelements.com/compounds/cobalt/cobalt_oxide.html, November 2016.

[12] SI Csiszar et al. Controlling orbital moment and spin orientation in CoO layers by strain. *Physical Review Letters*, 95(18):187205, 2005.

[13] Diffraction and Positioning Equipment: Diffractometer to Synchrotron Application. http://www.xhuber.de/en/, December 2016.

[14] Larry L Howell. *Compliant Mechanisms*. John Wiley & Sons, 2001.

[15] Nicolae Lobontiu. *Compliant Mechanisms: Design of Flexure Hinges*. CRC press, 2002.

[16] Jonathan Hopkins and Martin Culpepper. Synthesis of multi-degree of freedom, parallel flexure system concepts via Freedom and Constraint Topology (FACT) - Part I: Principles. *Precision Engineering*, 34(2):259–270, 2010.

[17] Ethan Burnham-Fay and Jonathan Ellis. Precision flexure stage utilizing parasitic motion.

[18] Shouzhong Li and Jingjun Yu. Design principle of high-precision flexure mechanisms based on parasitic-motion compensation. *Chinese Journal of Mechanical Engineering*, 27(4):663–672, 2014.

[19] The Origins of the Finite Element Method. University of Colorado. http://www.colorado.edu/engineering/cas/courses.d/IFEM.d/IFEM.AppO.d/IFEM.AppO.pdf, December 2016.

[20] António Ferreira. *MATLAB Codes for Finite Element Analysis: Solids and Structures*, volume 157. Springer Science & Business Media, 2008.

[21] The Plane Stress Problem. University of Colorado. http://www.colorado.edu/engineering/cas/courses.d/IFEM.d/IFEM.Ch14.d/IFEM.Ch14.pdf, December 2016.

[22] Solve partial differential equations using Finite Element Analysis. https://www.mathworks.com/products/pde.html, December 2016.

[23] Xavier Fayolle et al. Controlling testing machines with digital image correlation. *Experimental Techniques*, 31(3):57–63, 2007.

[24] Bruce Lucas and Takeo Kanade. An iterative image registration technique with an application to stereo vision. 1981.

[25] Michael Sutton et al. *Image correlation for shape, motion and deformation measurements: basic concepts, theory and applications*. Springer Science & Business Media, 2009.

[26] Zheng-Zong Tang et al. Photogrammetry-based two-dimensional digital image correlation with nonperpendicular camera alignment. *Optical Engineering*, 51(2):023602–1, 2012.

[27] Keysight Technologies. Atomic Force Microscopy - What is it? http://www.keysight.com/main/editorial.jspx?ckey=1774141&lc=por&cc=BR, November 2016.

[28] Miho Yasaka. X-ray thin-film measurement techniques. *The Rigaku Journal*, 26(2), 2010.

[29] Jens Als-Nielsen. *Elements of Modern X-ray Physics*. John Wiley & Sons, 2011.

[30] Mario Birkholz. *Thin Film Analysis by X-ray Scattering*. John Wiley & Sons, 2006.

[31] B D Cullity. *Elements of X-ray Diffraction*. Addison-Wesley Publishing Company, 1957.

[32] Sharonl Mitchel and Javier Pérez-Ramírez. X-ray diffraction. Surface Science and Methods in Catalysis. ETH Zürich, Institute for Chemical and Bioengineering - lectures.

[33] Stavax stainless properties. http://www.uddeholm.com/files/PB_Uddeholm_stavax_esr_english.pdf, February 2017.

[34] Precision Engineering - Leaf Spring Reinforced. http://www.janssenprecisionengineering.com/page/flexure-guiding-2-leaf-springs-in-parallel/, February 2017.

[35] XOP - Synchrotron Data Visualization and Analysis. http://www.esrf.eu/home/UsersAndScience/support-and-infrastructure/software/data-analysis/xop2.4/extensions.html, October 2016.